

1 Evolution of the firn pack of Kaskawulsh Glacier, Yukon: meltwater 2 effects, densification, and the development of a perennial firn aquifer

3
4 Naomi Ochwat¹, Shawn Marshall^{1,2}, Brian Moorman¹, Alison Criscitiello,³ Luke Copland⁴

5 ¹Department of Geography, University of Calgary, Calgary, Alberta, T2N 1N4, Canada

6 ²Environment and Climate Change Canada, Gatineau, Quebec, K1A 0H3, Canada

7 ³Department of Earth and Atmospheric Sciences, University of Alberta, Edmonton, T6G 2R3, Canada

8 ⁴Department of Geography, Environment and Geomatics, University of Ottawa, Ottawa, Ontario K1N 6N5, Canada

9
10 *Correspondence to:* Naomi Ochwat (naomi.ochwat@ucalgary.ca)

11
12 **Abstract.** In spring 2018, two firn cores (21 m and 36 m in length) were extracted from the accumulation zone of
13 Kaskawulsh Glacier, St. Elias Mountains, Yukon. The cores were analyzed for ice layer stratigraphy and density, and
14 compared against historical measurements made in 1964 and 2006. Deep meltwater percolation and refreezing events were
15 evident in the cores, with a total ice content of 2.33 ± 0.26 m in the 36-m core and liquid water discovered below a depth of
16 34.5 m. Together with the observed ice content, surface energy balance and firn modelling indicate that Kaskawulsh Glacier
17 firn retained about 73% of its meltwater in the years 2005-2017. For an average surface ablation of $0.38 \text{ m w.e. yr}^{-1}$ over this
18 period, an estimated $0.17 \text{ m w.e. yr}^{-1}$ refroze in the firn, $0.065 \text{ m w.e. yr}^{-1}$ was retained as liquid water, and $0.105 \text{ m w.e. yr}^{-1}$
19 drained or ran off. The refrozen meltwater is associated with a surface lowering of 0.73 ± 0.23 m between 2005 and 2017
20 (i.e., surface drawdown that has no associated mass loss). The firn has become denser and more ice-rich since the 1960s, and
21 contains a perennial firn aquifer (PFA), which may have developed over the past decade. This illustrates how firn may be
22 evolving in response to climate change in the St. Elias Mountains, provides firn density information required for geodetic
23 mass balance calculations, and is the first documented PFA in the Yukon-Alaska region.

25 1 Introduction

26 With the increasing effects of climate change and the need for understanding glacier and ice sheet melt rates, geodetic
27 methods are useful for indirect measurements of mass balance (Cogley, 2009). Based on repeat altimetry, geodetic
28 approaches to mass balance monitoring rely on several assumptions. Estimates must be made of the density of snow, firn,
29 and ice at the sampling location, with the additional assumption that these densities remain unchanged between the two
30 measurement dates. However, over multi-annual timescales in a warming climate this may not be true (Moholdt et al.,
31 2010b). Meltwater percolation and refreezing can significantly change the firn density profile and mean density of the
32 accumulation zone of a glacier (Gascon et al., 2013), and can introduce large uncertainties when using geodetic techniques to
33 determine glacier mass balance if they are not properly accounted for. For example, Moholdt et al. (2010a) determined the
34 geodetic mass balance of Svalbard glaciers to be $-4.3 \pm 1.4 \text{ Gt yr}^{-1}$, based on ICESat laser altimetry, with the large
35 uncertainty attributed to limited knowledge of the snow and firn density and their spatial and temporal variability. By
36 altering the density and causing surface lowering, meltwater percolation, refreezing, and liquid water storage all complicate
37 the interpretation of geodetic mass balance data.

38

39 Warming firn can result in increased meltwater production and altered firn densification processes. Initially, melt can round
40 the snow grains and increase the snowpack density. Meltwater can percolate into the firn and refreeze as ice layers or lenses.
41 On glaciers with medium to high surface melt, and high annual snow accumulation, meltwater that percolates below the
42 winter cold layer often will not refreeze, and may thus form a perennial firn aquifer (PFA) if this water cannot effectively
43 drain through crevasses or moulins (Kuipers Munneke et al, 2014). These internal accumulation processes can significantly
44 increase the firn density, and once ice layers or PFAs form they affect how meltwater percolates through the firn pack
45 (Gascon et al., 2013). Due to the spatial heterogeneity of meltwater retention, percolation, and refreezing processes, there are
46 still many gaps in knowledge of how to model these processes and subsequently estimate firn density in areas where these
47 processes occur (van As et al., 2016).

48

49 Meltwater retention in firn is also important for estimating glacial runoff contributions to sea level rise. Numerous recent
50 studies have investigated meltwater refreezing processes in northern locations such as southern Greenland (Humphrey et al.,
51 2012; Harper et al., 2012; De La Peña et al., 2015; MacFerrin et al., 2019), Canadian Arctic Archipelago (Noël et al. 2018,
52 Zdanowicz et al., 2012; Bezeau et al., 2013; Gascon et al., 2013), and Svalbard (Noël et al. 2020, Van Pelt et al., 2019,
53 Christianson et al., 2015). In many locations, short term increases in surface melt rates may not result in proportional
54 increases in surface runoff due to percolation and refreezing of meltwater in the firn pack (e.g., Harper et al., 2012; Koenig et
55 al., 2014; MacFerrin et al., 2019). However, in the long term this may lead to expansion of low-permeability ice layers,
56 causing run-off to increase and expediting the movement of water from glaciers to the ocean (MacFerrin et al., 2019,

57 Machguth et al., 2016). Current knowledge of these processes is limited for mountain glaciers in other regions, although this
58 information is required for improved estimates and models of glacier mass balance and associated sea-level rise.

59

60 In this study two firn cores were retrieved in spring 2018 on Kaskawulsh Glacier, St. Elias Mountains, Yukon, and analyzed
61 for density and the effects of meltwater percolation and refreezing. Comparisons of these measurements with firn density
62 profiles and temperatures collected at a nearby site in 1964 and 2006 enable us to: (i) Quantify contemporary firn
63 characteristics and densification processes; (ii) Determine how the physical properties of the firn pack have changed over the
64 past ~50 years; and (iii) Assess the likelihood of a widespread PFA on the upper Kaskawulsh Glacier.

65 **2 Study area**

66 The St. Elias Mountains are located in the southwest corner of Yukon Territory, Canada, and contain many peaks higher than
67 3000 m, including the highest mountain in Canada, Mount Logan, at 5959 m a.s.l. (Figure 1). The St. Elias is home to the
68 largest icefield outside of the polar regions, with an area of ~46,000 km² (Berthier et al., 2010). Measurements presented
69 here are focused on the upper accumulation zone of Kaskawulsh Glacier (Figure 1), which is part of an extensive (~63 km²)
70 snowfield at an elevation of 2500-2700 m a.s.l. This plateau region has subtle topographic variations and includes the
71 drainage divide between the Kaskawulsh and Hubbard Glaciers.

72

73 Kaskawulsh Glacier is a large valley glacier located on the eastern side of the St. Elias Mountains within the Donjek Range,
74 and is approximately 70 km long and 3-4 km wide. Our 2018 drill site was located on the upper north arm of the glacier in
75 the accumulation zone (60.78°N, 139.63°W), at an elevation of 2640 m a.s.l. Based on satellite imagery, Foy et al. (2011)
76 estimated an average equilibrium line altitude (ELA) for the glacier of 1958 m a.s.l. for the period 1977-2007, while Young
77 et al. (2020) provided a mean ELA of 2261 ±151 m a.s.l. for the years 2013-2019. Our core site is thus well above the ELA,
78 and has remained within the main accumulation area of the glacier. Mean annual and summer (JJA) air temperatures from
79 1979-2019 were -10.7°C and -2.5°C, respectively, based on bias-adjusted ERA5 climate reanalyses (Hersbach et al., 2020).
80 The main melt season occurs from June through August. Over the period 1979-2016, Williamson et al. (2020) reported that
81 the St. Elias Icefield air temperature warmed at an average rate of 0.19°C decade⁻¹ at an elevation of 2000-2500 m a.s.l.,
82 rising to 0.28°C decade⁻¹ at an elevation of 5500-6000 m a.s.l.

83

84 Previous studies of Kaskawulsh Glacier have included an analysis of volume change over time based on comparisons of
85 satellite imagery and digital elevation models (Foy et al., 2011; Young et al., 2020). Several reports in the 1960s documented
86 various glaciological characteristics and processes occurring in the St. Elias Icefields, as part of the Icefield Ranges Research
87 Project (IRRP) (Wood, 1963; Grew and Mellor, 1966; Marcus and Ragle, 1970). Firn density and temperature measurements
88 to 15-m depth were made during this period at site IRRP A, near the Kaskawulsh-Hubbard divide and about 5 km from our

89 core site. Additional snow accumulation data are available from the ‘Copland Camp’ site on the upper Hubbard Glacier,
90 located ~12 km southwest of our drill site and at a similar elevation (Figure 1). A weather station located on a nunatak near
91 to Copland Camp has been in service since 2013 (60.70°N, 139.80°W, ~2600 m a.s.l.; Figure 1). Other relevant studies in the
92 region include ice cores collected from the Eclipse Icefield, located 12 km northwest of our drill site (Yalcin et al., 2006;
93 Zdanowicz et al., 2014) but at a higher elevation (3017 m a.s.l.).

94

95 We consider snow accumulation rates, weather conditions, and earlier firn core studies across several different locations
96 within this broad snowfield region that constitutes the upper accumulation areas of the Kaskawulsh and Hubbard Glaciers.
97 Some caution is needed in comparing different sites, but the region is relatively flat and uniform, with the exception of some
98 nunataks. Away from the nunataks there is negligible influence from topographic obstacles or valley walls, so we
99 hypothesize that the upper accumulation area will be exposed to similar climate conditions and snow accumulation rates over
100 long periods. The possibility of significant spatial variability cannot be ruled out, however, so we consider this further in the
101 data analysis.

102

103 **3 Methods**

104 **3.1 Ice core field collection**

105 Two 8-cm diameter cores were drilled between May 20th and 24th, 2018, using an ECLIPSE ice drill (Icefield Instruments,
106 Whitehorse, Yukon). With a starting depth of 2 m below the snow surface, Core 1 was 34.6 m long and reached a depth of
107 36.6 m, and Core 2 was 19.6 m long and reached a depth of 21.6 m. The two cores were drilled 60 cm apart, and core
108 stratigraphy and density were recorded in the field. At a depth of 34.5 m below the snow surface, liquid water became
109 evident in Core 1; drilling was stopped at a depth of 36.6 m to avoid the risk of the drill freezing in the hole.

110

111 Once the cores were retrieved the presence of ice layers, ice lenses and “melt-affected” firn was logged and the stratigraphic
112 character (e.g., texture, opacity), depth, and thickness were recorded. Melt-affected firn refers to any firn that displays
113 physical characteristics indicating that there was the presence of liquid water at some point (Figure S5). This can result in ice
114 layers, ice lenses, or can be indicated by the lack of grain boundaries, the presence of air bubbles, and opacity. When an ice
115 horizon extended across the entire diameter of the core, it was labeled as an ice layer. If the ice horizon was of more limited
116 lateral extent, it was labeled an ice lens. Ice lenses were occasionally wedge shaped.

117

118

119

120

121
122
123
124
125
126
127
128
129
130

All of the density measurements for Core 1 were completed in the field. The Core 2 samples could not be measured for density in the field due to lack of time, so were flown to Kluane Lake Research Station frozen, where the measurements were made within 24 hours of arrival. A random assortment of 125 out of the 196 Core 2 sample bags were damaged during this transport, so were not included in the measurements. This left 71 samples available to use for the density analysis, with at least one sample available per meter except for between 13.29 and 14.95 m. Due to these missing values, only bulk density values are presented for Core 2.

131 3.2 Ice core density analysis

132 Ice core density measurements were completed in the field. Each core was sawed into ~10-cm long sections in the field, and
133 the diameter of the sections measured at each end. The sections were then double bagged, weighed, and assessed for the
134 quality of the core sample and its cylindrical completeness, which we denote f . The average diameter was used to determine
135 the volume of the core section (V). Together with the mass of the core section, m , density was calculated following:

136
137
$$\rho = m/V, \text{ with } V = f\pi L(D/2)^2, \tag{1}$$

138
139 where ρ is the density of the firm, D is the average core section diameter, L is the length of the section, and $f \in [0,1]$ is the
140 subjectively assessed fraction of completeness of the core section. For example, if visual inspection indicated that about 5%
141 of the core was missing (e.g., due to missing ice chips caused by the core dogs of the drill head), then f would be 0.95.
142 Outliers were removed for the background firm density calculations if they were not physically possible (i.e., values $>917 \text{ kg}$
143 m^{-3} or $<300 \text{ kg m}^{-3}$ at depths below the last summer surface). Outliers from 32-36 m depth had residual liquid water in them,
144 so these higher density values were retained.

145
146 In order to calculate the uncertainty in density, $d\rho$, random and systematic sources of error have to be taken into account in
147 the propagation of errors:

148
$$d\rho = \rho \sqrt{\left(\frac{dm}{m}\right)^2 + \left(\frac{dV}{V}\right)^2} . \tag{2}$$

149 The mass uncertainty was assumed to be 0.3 g, which is a conservative estimate given the scale's accuracy ($\pm 0.1 \text{ g}$), but
150 accounts for potential residual snow or water on the scale. The volume uncertainty is calculated by breaking down Eq. (1) for
151 sample volume, $V = fAL$, where cross-sectional area $A = \pi(D/2)^2$. There is uncertainty in the measured length of the core

152 section, L , the radius of the core section, $D/2$, and the assessment of the completeness of the core sample, f . Each of these
 153 was calculated independently and the propagation of uncertainty was calculated from:

154

$$155 \quad dV = V \sqrt{\left(\frac{df}{f}\right)^2 + \left(\frac{dA}{A}\right)^2 + \left(\frac{dL}{L}\right)^2} . \quad (3)$$

156 dL was assumed to be 0.25 cm because the tape measure had ticks at every mm so it could be measured with precision, but
 157 core sections were often uneven, with crumbly edges caused by the drill cutters. The same uncertainty was assigned to the
 158 measurement of core diameter. Given two independent measurements, the uncertainty in the diameter is $dD =$
 159 $\frac{1}{2}\sqrt{(0.25)^2 + (0.25)^2} = 0.18$ cm. For the cross-sectional area, the uncertainty $dA = \pi DdD/2$.

160

161 Values of f were determined by assessing the shape of the core and deciding how complete a cylinder the core section
 162 represented (e.g., accounting for missing volume due to chips from the core dogs along the edges). Three different people
 163 performed this evaluation, so there was subjectivity in each of the f values and it is best to be conservative with this estimate.
 164 We assigned this to be $df = 0.2$ for $f < 0.8$ and $df = 0.1$ for $f \geq 0.8$. The uncertainty of a higher f value is lower, because when
 165 a core was of good quality it was obvious. Less complete cylinders were more difficult to assess, hence the greater
 166 uncertainty when $f \leq 0.8$. The f value has the greatest effect on the overall uncertainty calculation for firn density. We did not
 167 record f values for Core 2 in the field, so values are based on the measurements from Core 1. The minimum value recorded
 168 in Core 1 was $f = 0.7$, with a maximum of 1 and an average of 0.96. We assume a value of $f = 0.96 \pm 0.1$ for all of Core 2.

169

170 The resulting uncertainty in the density was calculated from:

$$171 \quad d\rho = \rho \sqrt{\left(\frac{dm}{m}\right)^2 + \left(\frac{dV}{V}\right)^2} . \quad (4)$$

172 For the average densities, $\bar{\rho}$, the uncertainty can be calculated from the standard error of the mean, $d\bar{\rho} = d\rho/\sqrt{N}$, for sample
 173 size N . This can be estimated from the average value of $d\rho$, but we report the more precise uncertainty calculated from the
 174 root-mean square value of all point values, $d\bar{\rho} = \frac{1}{N}[\sum_N d\rho_k^2]^{1/2}$. Density can be expressed as water equivalence (w.e.)
 175 for each core section from the conversion $w = L\rho/\rho_w$, where ρ_w is the density of water. For the whole core, of length L_c , the
 176 water equivalence is $w_c = L_c\bar{\rho}/\rho_w$, with units m w.e. We also include an estimate of the age of the cores, based on an
 177 estimate of the average annual net accumulation rate, \bar{a} , with units m w.e. yr⁻¹. The age of the core is then $\tau_c = w_c/\bar{a}$.
 178 Uncertainty is estimated by propagation of uncertainties in w_c and \bar{a} . We use an uncertainty of $dL_c = 0.5$ m for the total
 179 length of the core, L_c , which is based on measurements during retrieval of Core 1 of 35.05 m from the drill panel, 34.59 m

180 from the addition of core lengths, and 34.25 m from the sum of the ~10 cm samples. For Core 2 the length was 19.75 m from
181 the drill panel, 19.35 m from the addition of core lengths, and 19.63 m from the sum of the ~10 cm samples.

182

183 Ice fraction, $F_i \in [0,1]$, was calculated for each 10-cm section of the firn core. Here ice was defined based on its lack of air
184 bubbles and crystalline structure, as compared to the granular structure of firn. We refer to this as ice fraction, rather than
185 melt percent, as melt percent generally assumes that the meltwater remains within the net annual accumulation layer
186 (Koerner, 1977), which cannot be assumed here due to evidence that meltwater percolates beyond the annual accumulation
187 layer and refreezes into previous years' accumulation. The thickness of individual ice layers was summed within each 10-cm
188 core section. In core samples that had ice lenses, their diameter typically occupied about 50% of the core sample; therefore
189 their thickness was divided by two before being summed. For each core section, total ice content was divided by the length
190 of the section, L , to give F_i . These values were also summed to give the total ice core ice content.

191

192 To understand the firn densification process in the absence of refrozen meltwater, the 'background' firn density is of interest.
193 For each sample, we estimated this by subtracting the mass and volume of the ice to give the firn density in the absence of
194 ice content. We used a 30-cm moving average of total ice content and density in order to smooth out a possible error of ± 10
195 cm in assigning the location of the ice features within the stratigraphy. Each sample had a measured bulk density, ρ_b , which
196 we assume resulted from a binary mixture of ice and firn, with densities ρ_f and ρ_i . Ice and firn fractions, F_i and F_f , were
197 defined with $F_i + F_f = 1$. The background firn density was then calculated following:

198

$$\rho_f = (\rho_b - \rho_i F_i) / F_f. \quad (5)$$

199 In cases where there was no ice fraction ($F_i = 0$), $\rho_f = \rho_b$. Ice layers and lenses were assumed to have a density of 874 ± 35
200 kg m^{-3} , based on the average density of firn-core sections that were 100% ice in Greenland (873 kg m^{-3}) and Devon Ice Cap
201 (875 kg m^{-3}) (Bezeau et al., 2013; Machguth et al., 2016). This is different from the 917 kg m^{-3} upper bound used in the
202 outlier analysis because that is the theoretical limit for pure ice, whereas 874 kg m^{-3} is based on measured field data which
203 includes observed ice layers and lenses which have small bubbles and imperfections in them.

204

205 There is surface lowering associated with melting but without associated mass loss, due to subsurface refreezing. This
206 surface lowering is an 'apparent ablation' in airborne or satellite altimetry signals. We calculated this for each core section
207 using the background firn density, ρ_f , and length of the section, L . The 'thinning' or surface lowering of a given core
208 section, ΔL , was estimated by reverting the ice to the density of the background firn, following:

209

210

$$\Delta L = L \left[\left(F_f + \frac{\rho_i F_i}{\rho_f} \right) - 1 \right]. \quad (6)$$

211 Summed over the full firn column, this gives the total surface lowering associated with meltwater that percolates and
212 refreezes, with no actual loss of mass.

213

214

215

216 **3.3 Historical measurements**

217 As part of an expedition undertaken by the IRRP, Grew and Mellor (1966) measured snow density and temperature to a
218 depth of 15 m at the Divide site on July 23, 1964 (Fig. 1). The first ~4 m were measured in a snow pit, while the remaining
219 ~11 m were based on measurements of a core drilled with a Cold Regions Research and Engineering Laboratory (CRREL)
220 coring auger. The original data is not available, so values were reconstructed based on digitization of the density plot
221 provided in Figure 4 of Grew and Mellor (1966). This digitization was undertaken with WebPlot Digitizer 4.3 (Rohatgi,
222 2020), and has an estimated error of $\pm 2 \text{ kg m}^{-3}$ for density and $\pm 0.01 \text{ m}$ for depth. Errors were calculated by clicking the
223 same point 25 times and evaluating the variability of the points (i.e., the standard deviation).

224

225 From July 14-17, 2006, snow density and temperature measurements were recorded every 10 cm to a depth of 10.4 m at the
226 Copland Camp as part of a University of Ottawa field class. Measurements from 0 to 5.4 m were recorded in a snow pit,
227 while those from 5.5 to 10.4 m were based on a core recovered with a Kovacs Mark II coring system (Kovacs Enterprises,
228 Oregon, USA). Density measurements in the snow pit were undertaken with a 250 cm³ RIP 2 Cutter (Snowmetrics,
229 Colorado, USA), and in the ice core by measuring and weighing core sections and using Eq. (1). Errors in the density
230 measurements were determined from Eq. (4), and verified against density values recorded in a second snow pit dug to a
231 depth of 4.0 m, approximately 2 m away from the first. All temperature measurements were undertaken with a Thermor
232 PS100 digital stem thermometer with an accuracy of $\pm 0.5^\circ\text{C}$.

233

234 Annual snow accumulation at the Copland Camp was measured between 2004-2011 with a Campbell Scientific SR50 Sonic
235 Ranging Sensor mounted on a cross-arm on a vertical steel pole drilled into the firn. The SR50 was connected to a Campbell
236 Scientific CR10X logger, and included a correction for the change in speed of sound with air temperature. The mounting
237 pole was raised annually to keep it above the snow surface, and densities recorded in snow pits collected during annual
238 University of Ottawa field classes (typically in early July) were used to convert the SR50 depth measurements into w.e.
239 values.

240

241 **3.4 Energy balance and firn modelling**

242 ERA climate reanalyses were used to examine changes in climate and annual surface melting at the study site since the
243 1960s, coupled with a firn model to simulate the decadal evolution of firn temperature, hydrology, ice content, and density.
244 Daily melt rates were calculated from 1965 to 2019 using a surface energy balance model (Ebrahimi and Marshall, 2016),
245 coupled to a subsurface model of coupled thermal and hydrological evolution in the snow and firn (Samimi et al., 2020). The
246 model calculates the surface energy budget and snow melt based on incoming shortwave and longwave radiation,
247 temperature, relative humidity, wind speed, and air pressure, with internal parameterizations of surface albedo evolution and
248 outgoing longwave radiation. Conductive heat flux to the snow surface and snow surface temperatures are simulated within
249 the subsurface snow/firn model. Snow and firn densification are parameterized following Vionnet et al. (2012) for the firn
250 matrix ('background firn'), with bulk density including the additional mass of any ice or water content. Details of the model
251 are provided in the Supplementary Information.

252

253 Meteorological inputs for the surface energy balance model were derived from the ERA5 climate reanalysis for the period
254 1979 to 2019 (Hersbach et al., 2020), and extended back to 1965 using the ERA 20th century reanalysis (ERA20c; Poli et al.,
255 2016). ERA5 outputs are at a resolution of 0.25° latitude and longitude, and data for our analysis was averaged from ERA5
256 grid cells located at (60.75°N, 139.75°W) and (60.75°N, 139.5°W). ERA20c data are at 1° latitude and longitude resolution,
257 and we interpolated meteorological conditions to the upper Kaskawulsh Glacier from the four model grid cells at 60°
258 61°N and 139° to 140°W. ERA20c fields were homogenized with ERA5 through bias adjustments for two years of overlap
259 in the reanalyses, 1979 and 1980, with ERA5 assumed to be the more accurate reconstruction. Monthly bias adjustments
260 based on this period of overlap were then applied to the ERA20c data from 1965 to 1978.

261

262 The reanalysis data represent the climatology over the region of the upper Kaskawulsh-Hubbard divide (i.e., a 0.25° grid
263 cell), and are not specific to our core site. The firn modelling is therefore taken to be generally applicable for this upper
264 plateau region. However, ERA meteorological conditions (temperature, pressure, humidity) are bias-adjusted to the specific
265 elevation of our core site, 2640 m. ERA5 temperature fields were evaluated against Copland weather station data from 2014-
266 2018, which indicate a small (0.6°C) cold bias in the ERA5 data for average summer (JJA) temperatures over this period.
267 ERA temperatures were further bias-adjusted by this amount. Our core site, the Copland weather station, Copland Camp, and
268 IRRP research sites all fall within the same ERA5 grid cell, and we make the assumption that climate conditions are similar
269 for similar elevations and glaciological settings within this region.

270

271 Surface energy balance and melt were calculated every 30 minutes, using mean daily meteorological forcing from ERA and
272 a parameterization of the diurnal cycles of temperature and incoming shortwave radiation (Ebrahimi and Marshall, 2016).

273 Subsurface temperatures were modelled for a 35-m firn column, with a simple model for meltwater percolation that accounts
274 for meltwater refreezing and the associated latent heat release where snow or firn is below 0°C (Samimi and Marshall, 2017;

275 Samimi et al., 2020). For the current study, we discretize the snow and firn into 58 layers from 0.1 to 1 m in thickness, with
276 higher resolution near the surface. The firn model is coupled with the surface energy balance model, solving for the firn
277 thermodynamic and hydrological evolution at 30-minute time steps for the period 1965 to 2019. The subsurface temperature
278 evolution includes vertical heat conduction and latent heat release from refreezing. When subsurface temperatures reach 0°C,
279 liquid water is retained or percolates to depth, following a Darcian parameterization for water flux: $q_w = -k_h \nabla \phi$, for hydraulic
280 conductivity k_h and hydraulic potential ϕ (Samimi and Marshall, 2017). For the numerical experiments in this study we set k_h
281 = 10^{-5} m s⁻¹ in snow and 10^{-6} m s⁻¹ for snow and firn, respectively. Capillary water retention is calculated following Coléou
282 and Lesaffre (1998). The default model parameters are based on calibration at DYE-2, Greenland, in the percolation zone of
283 the southern Greenland Ice Sheet (Samimi et al., 2020). A broader range of model parameters is explored in sensitivity
284 analyses presented in the Supplementary Information.

285

286 The model is ‘spun up’ through a 30-year simulation with perpetual 1965 climate forcing (i.e., running through 30 annual
287 cycles with 1965 climate conditions). This provides the initial temperature, density, and ice-layer structure within the firn
288 column. Sensitivity tests within the Supplementary Information also examine the model sensitivity to these initial conditions
289 and the spin-up assumptions.

290

291 **4 Results**

292 **4.1 Ice core density**

293 The density data are plotted in Figure 2, fitted with a logarithmic curve to quantitatively compare our two cores. The first 4.2
294 m of both 2018 cores was dry and had an average density of 450 ± 21 kg m⁻³, with no ice content. At 4.2 m there was a
295 significant ice crust, with large crystal size, rounded grains and high impurity content, which was assumed to represent the
296 last summer surface (LSS) from 2017. The snow above this LSS layer was therefore classified as seasonal snow. In this
297 section we focus on the firn characteristics below the LSS, so our discussion is centered on the core recovered between 4.2
298 and 36.6 m below the surface for Core 1 (i.e., total firn length of 32.4 m), and between 4.2 and 21.6 m below the surface for
299 Core 2 (i.e., total firn length of 17.4 m). For consistency, we reference all depths to the seasonal snow surface throughout
300 this paper.

301

302 In the upper 10 m of firn (4.2 to 14.2 m below the surface; Table 1), Cores 1 and 2 had average densities of 588 ± 8 kg m⁻³
303 and 572 ± 7 kg m⁻³, respectively, giving an overall average density of 580 ± 5 kg m⁻³. Over the upper 17.4 m of firn in each
304 core (4.2 m to 21.6 m below the surface; the depth to the bottom of Core 2), Kaskawulsh firn had an average density of 632
305 ± 4 kg m⁻³. The full 32.4 m of firn at Core 1 (4.2 to 36.6 m below the surface) had an average density of 698 ± 5 kg m⁻³. Ice
306 content generally increased with depth in the upper ~25 m of the core, but deeper sections were less icy (Table 1). The

307 bottom 5 m of firn in Core 1 had an average density of $826 \pm 13 \text{ kg m}^{-3}$, but with no identified ice layers. Based on the high
308 density and texture of this deep firn, along with the presence of liquid water in the deepest sections of the core, we believe
309 that we drilled to near the base of the firn at the core site, but cannot confirm this as we halted drilling before reaching
310 glacier ice.

311

312 Total ice content in the 32.2 m firn portion of Core 1 (4.2 to 36.6 m below the surface) was $2.33 \pm 0.26 \text{ m}$ of ice or $2.67 \pm$
313 0.24 m w.e. This is equivalent to 7.2% by volume and 11.9% by mass (Table 1). Using Eq. (5) and the values for ice content
314 in Core 1, we estimate a background firn density of $676 \pm 6 \text{ kg m}^{-3}$ for the full column of firn, 3.2% less than the bulk density
315 of the firn (Table 1). The two cores had very similar bulk and background densities over the upper 10 m of firn (4.2 to 14.2
316 m below the surface) and 17.4 m (4.2 to 21.6 m below the surface), where a direct comparison was possible. The total water
317 equivalent of firn in Core 1 was calculated to be $w_c = 22.5 \pm 0.2 \text{ m w.e.}$

318

319 4.2 Ice core stratigraphy

320 The stratigraphy of the 2018 cores indicates numerous ice layers as well as melt-affected firn, distinguished by a lack of
321 grain boundaries or opaque, bubbly firn. The first 4.2 m comprised the seasonal snowpack, with firn below. Within the first 6
322 m below the surface there were several small ice layers (<2.5 cm thick), interpreted as wind crusts (Figure 3). Several thick
323 (>10 cm) ice layers were found between 6 and 26 m depth (1.8 to 21.8 m in the firn). The largest ice layer in Core 1 was 22
324 cm thick, found at 14.1 m (9.9 m in the firn). At 26.4 m (22.2 m in the firn) the ice layers and lenses disappeared. Below this
325 the firn was almost entirely meltwater-affected, based on its appearance and texture, but without the quantity of ice lenses or
326 ice layers that were present in the first 25 m. We interpret this section of the core as infiltration ice, consisting of water-
327 saturated firn that has experienced refreezing. At 30 m depth (25.8 m in the firn), the meltwater effects were absent and there
328 were two small ice layers and an ice lens. At 30.6 m depth the firn was melt-affected again. From 34.5 to 36.6 m (30.3 to
329 32.4 m in firn) the core sections expelled liquid water as they were extracted from the core barrel.

330

331 In Core 2 there were numerous ice layers starting at a depth of 3.8 m, and below 4.4 m (0.2 m in the firn) the core was
332 meltwater-affected. There was a thick ice layer at 6.6 m (2.4 m in the firn) that was 30 cm lower than a similar ice layer in
333 Core 1 at 6.3 m. There were numerous melt-affected layers between ice lenses much closer to the surface in Core 2 than
334 Core 1. In Core 1 there were several ice layers at ~10 m depth (5.8 m in the firn), but these layers were not present in Core 2.
335 At 14.4 m (10.2 m in the firn) another section of the firn had numerous ice layers (~20-30 cm deeper than recorded in Core
336 1), and at 14.6 m the thickest ice layer was encountered (12 cm), corresponding well with the thickest layer in Core 1.
337 Between 16 and 21.5 m (11.8 to 17.3 m in the firn) the core was melt-affected. We attribute differences between Core 1 and
338 Core 2 stratigraphy to uncertainty in the depth of features (as discussed in Section 3.2), and horizontal variability in
339 meltwater infiltration, which is known to occur at length scales less than 1 m (Parry et al., 2007; Harper et al., 2011).

340

341 **4.3 Changes in firn characteristics over time**

342 The firn in the accumulation area of Kaskawulsh Glacier has become denser since 1964 (Figure 4a). The mean density of the
343 upper 7 m of firn was 516 kg m^{-3} in 1964 (3.3 to 10.3 m below the surface), 590 kg m^{-3} in 2006 (3.5 to 10.5 m below the
344 surface) and 549 kg m^{-3} in 2018 (4.4 to 11.4 m below the surface). The difference between the average densities from the
345 upper 7 m in the 1964 and 2018 core is 33 kg m^{-3} , which is an increase of $\sim 7\%$. It is difficult to assess whether firn
346 temperatures have changed over this time, as limited data are available from below the depth of the annual temperature wave
347 ($\sim 10 \text{ m}$ for heat diffusion, and deeper than this with the effects of subsurface meltwater infiltration and latent heat release).
348 Borehole temperature records from Grew and Mellor (1966) indicate temperate (0°C) conditions at 15-m depth in the
349 summer of 1964, which suggests that deep temperate firn may have existed at this site in the 1960s. This supports the
350 assumption that Kaskawulsh Glacier is temperate (Foy et al., 2011), despite mean annual air temperatures of about -11°C on
351 the upper glacier.

352

353 Accumulation data from the IRRP A site, Copland Camp and our 2018 measurements do not show any evidence for a
354 significant change over time, although there can be high interannual variability. At IRRP A, Wagner (1969) reported values
355 between 1.3 m to 1.9 m w.e. yr^{-1} for 1963. Marcus and Ragle (1970) measured a winter snow accumulation of 1.6 m w.e.
356 from 1964-1965. Holdsworth (1965) reported an estimated mean annual accumulation rate of 1.8 m w.e. yr^{-1} in the early
357 1960s (year not specified) (Holdsworth, 1965). Yearly snow accumulation data from 2004-2011 collected with the SR50 at
358 Copland Camp indicate a mean annual accumulation rate of 1.77 m w.e. yr^{-1} , with variations between 1.3 and 2.4 m w.e. yr^{-1} .
359 The seasonal snowpack at our drill site was 4.2 m in May 2018, with an average snow density of 440 kg m^{-3} , giving a total
360 accumulation of 1.85 m w.e. for 2017-18.

361

362 Based on the above review, we adopt an estimate of $\bar{a} = 1.8 \pm 0.2 \text{ m w.e. yr}^{-1}$ for the net accumulation from 2005 to 2018.
363 Using this value, the firn layer of Core 1 represents 12.5 ± 1.4 years of net accumulation (i.e., 2005-2017), or 13.2 ± 1.4 years,
364 if the seasonal snowpack on top is counted. Over 12.5 years, the total measured ice content of 2.67 m w.e. in the firn equates
365 to an average meltwater refreezing rate of $0.22 \text{ m w.e. yr}^{-1}$.

366

367 **4.4 Surface energy balance and firn modelling**

368 Reconstructed air temperature, melt, and firn trends from 1965-2019 are shown in Figure 5. Summer air temperature from
369 the reanalysis (Figure 5A) shows a modest but statistically significant increase over the study period, with a trend of $+0.07^\circ\text{C}$
370 decade^{-1} . Table 2 reports changes in meteorological, energy balance, and modelled firn conditions over this time. Specific
371 humidity and incoming longwave radiation increase markedly over the 55 years, with trends of $+0.1 \text{ g kg}^{-1} \text{ decade}^{-1}$ and $+3.5$

372 $\text{W m}^{-2} \text{ decade}^{-1}$, respectively. This echoes the findings of Williamson et al. (2020), who report decadal-scale, high-elevation
373 warming in the St. Elias Mountains in association with increases in atmospheric water vapour and longwave radiation. These
374 trends augment the net energy available for melt, through increases in both the net radiation and latent heat flux. Modelled
375 annual melt averaged $230 \pm 210 \text{ mm w.e. yr}^{-1}$ from 1965 to 2019 and $380 \pm 310 \text{ mm w.e. yr}^{-1}$ from 2005 to 2017, 70% higher
376 than the long-term average. The latter interval represents the approximate period of record of the firn core. The trend in
377 surface melting is $+62 \text{ mm w.e. yr}^{-1} \text{ decade}^{-1}$ from 1965 to 2019 (Figure 5B). The summer of 2013 was exceptional; it had
378 the warmest summer temperatures on record, $T_{JJA} = -0.7^\circ\text{C}$, with 895 mm w.e. of meltwater (Table 2).

379
380 Within the model, 91% of the surface meltwater refreezes in the firn over the period 1965-2019, with 100% of it refreezing
381 in cool summers when meltwater generation is limited. Meltwater that does not refreeze percolates to depth in the firn
382 model. Figure 5B plots the annual melting minus refreezing, with positive values indicating deep percolation. If the firn is
383 temperate (0°C), meltwater can percolate through the entire depth of the firn column (35 m), where it is permitted to “drain”
384 through the lowest layer; this water leaves the system and is considered as runoff. Porewater in the firn also refreezes in the
385 subsequent winter, to the depth of the winter cold wave, accounting for the negative values in Figure 5B. This represents
386 percolated meltwater that refreezes within the firn column in the following calendar year. Complete meltwater retention is
387 typical for most of the period from 1965 to the early 2010s, but there is a marked increase in modelled runoff over the last
388 decade (Figure 5B), indicating drainage through the full 35-m firn column. Only 73% of surface melt refroze during the
389 period 2005-2017, and the mass loss associated with summer mass balance increased five-fold, from an average of -20 ± 120
390 mm w.e. yr^{-1} from 1965-2019 to $-105 \pm 220 \text{ mm w.e. yr}^{-1}$ from 2005-2017.

391
392 Summers with high amounts of surface melt produce greater refreezing and warming of the snow and firn, eventually
393 overwhelming the cold content and enabling deep percolation and drainage. Figures 5C and 5D plot the modelled evolution
394 of the firn temperatures and the wetting and melting fronts, which closely coincide. Snow and firn temperatures in Figure 5C
395 are mean annual values at the snow surface (the upper 0.1 m), and at 10, 20, and 35 m depth. For a purely conductive
396 environment, $\sim 10 \text{ m}$ represents the depth of the annual temperature wave (Cuffey and Paterson, 2010), but latent heat release
397 from meltwater refreezing warms the subsurface and causes a deeper influence of surface conditions, such that 10-m
398 temperatures are highly variable (Table 2). The modelled wetting and melting fronts in Figure 5D suggest dramatic recent
399 developments in firn thermal and hydrological structure at the Kaskawulsh drill site, with a regime shift in the firn structure
400 over the period 2013-2017. This is consistent with the birth of a deep PFA at this time. Figure 6 plots the full subsurface
401 temperature evolution over the period 1965-2019, showing the typical seasonal evolution of firn temperatures and the
402 unusual nature of the hydrological breakthrough event that began in 2013 and persists through 2019. Figures 5E and 5F plot
403 the modelled increases in average firn density and total firn ice content from 1965-2019. The average firn density in the
404 model is 682 kg m^{-3} in 2018, compared to $698 \pm 5 \text{ kg m}^{-3}$ measured in Core 1.

405

406 The model results in Figures 5 and 6 are for the ‘reference’ 1965-2019 ERA climatological forcing and firn model
407 parameters. These are the direct ERA climate fields, bias-adjusted to represent the elevation of the core site and to give
408 consistency with the regional Copland weather station data (2014-2018). The weather station has a similar elevation and
409 topoclimatic environment and is about 11 km from the core site, falling within the same ERA5 grid cell. Firn model settings
410 are based on calibrations against field data at DYE-2, Greenland, within the percolation zone of the southern Greenland Ice
411 Sheet (Samimi et al., 2020), but we have no local field calibration of these model parameters. There are therefore
412 uncertainties within both the climate forcing and the model parameters and assumptions. The Supplemental Information
413 examines the sensitivity of model results to several important meteorological inputs and model parameters, as well as the
414 strategy adopted for the model spin-up.

415

416 Select results are plotted in Figure 7, indicating the wide range of model behaviour that is possible with perturbations to the
417 model inputs, parameter settings, and spin-up assumptions. An air temperature anomaly of $\pm 1^\circ\text{C}$ applied to the reference
418 ERA climatology gives very different firn evolutions from 1965-2019, with warmer temperatures driving a shift to temperate
419 firn conditions in the late 1980s (Figures 7A and C). Warming of 2°C gives temperate firn for the entire period. In the other
420 direction, a temperature anomaly of -1°C is sufficient to maintain perpetual polythermal conditions at the site, precluding
421 the development of deep temperate firn or a PFA. Similar results are attained with perturbations of $\pm 10 \text{ W m}^{-2}$ to the
422 incoming longwave radiation (Supplemental Information). Increases in meltwater infiltration that are stimulated by lower
423 values of the irreducible water content ($\theta_{wi} < 0.025$) have a similar effect to warming, promoting meltwater infiltration, firn
424 warming, and the earlier development of temperate firn.

425

426 The simulations are also sensitive to the initial conditions (Figures 7B and D). Given evidence from Grew and Mellor (1966)
427 that firn at 15-m depth was temperate in the mid-1960s near our core site, we introduce temperature anomalies from $+0.5$ to
428 $+2^\circ\text{C}$ to the spin-up climatology. A perturbation of $+1.5^\circ\text{C}$ creates temperate conditions to 12-m depth, and $+2^\circ\text{C}$ is
429 sufficient to create deep temperate firn which persists for several years (Figure 7D). Firn refreezes in the 1970s within the
430 model, and eventually follows a similar path to the reference simulation, but with a memory of warmer initial firn
431 temperatures. This permits a more rapid transition (or return) to deep temperate conditions spurred by the heavy melt season
432 in 2013. Overall, the model sensitivities in Figure 7 indicate that a wide range of model solutions is possible at this site,
433 indicating that Kaskawulsh Glacier firn is very close to the threshold for either temperate or polythermal conditions. We
434 discuss this further below.

435

436 The initial firn density and ice content are relatively high when we force the model to produce temperate firn conditions in
437 the mid-1960s through an air temperature anomaly of $+2^\circ\text{C}$ in the model spin-up. Values in 1965 are 679 kg m^{-3} and 2.8 m,

438 compared with reference model values of 641 kg m^{-3} and 0.7 m. Figure 8 plots the subsequent firn temperature and density
439 evolution if the $+2^\circ\text{C}$ temperature anomaly is maintained from 1965 to 2019 and in the case where the model forcing is
440 restored to the reference ERA climatology from 1965 to 2019. Subsurface temperature and density evolutions in the latter
441 case parallel that of the reference model after a transient adjustment period of about a decade, while the perpetual $+2^\circ\text{C}$
442 anomaly maintains dense and temperate firn. The decadal adjustment of firn density (Figure 8B) is the ‘over-turning’ time of
443 the firn core, for downward advection of new snow and firn to 35 m depth. The temperature adjustment (Figures 8A,C) does
444 not follow this as it is governed by thermal diffusion time scales in the deep firn, giving a longer memory of the initial
445 conditions.

446

447 **5 Discussion**

448 **5.1 Firn characteristics and changes over time**

449 The accumulation area of Kaskawulsh Glacier currently has indications of widespread meltwater percolation and refreezing.
450 Meltwater is stored within the firn as ice, as indicated by the presence of ice layers and infiltration ice, and there is liquid
451 water at a depth of ~ 35 m below the surface. The density of the firn has increased by about 15% since 1964 in the first 7 m
452 of firn, due to the increased presence of ice layers. However, the firn in 1964 was not without meltwater percolation and
453 refreezing; Grew and Mellor (1966) note the presence of refrozen ice lenses and glands and report evidence for meltwater
454 infiltration and refreezing at depths of ~ 5 m. Nevertheless, the quantity and thickness of ice layers and lenses have increased
455 towards present day, as reflected in the changes in the stratigraphy and the density (Figure 4). The firn modelling also
456 indicates decadal-scale increases in firn ice content and density (Table 2, Figure 5E). For the reference model parameter
457 settings and ERA climate forcing, the model predicts a significant increase in melting (Figure 5B), driving increases in the
458 depth of the melting and wetting fronts, meltwater percolation and runoff, and latent heat release associated with refreezing
459 since the 1960s. This fundamentally changes the way the firn contributes to the mass balance of the glacier and englacial
460 hydrological dynamics, as discussed further in section 5.3. There are significant decadal firn warming trends in the model
461 (Figures 5 and 6), driven by the increases in melting and meltwater percolation. The modelling is not observationally
462 constrained, however (Figure 7 and Supplementary Material), so the simulated firn warming is uncertain.

463

464 Increased firn meltwater and ice content, as well as potential firn warming in recent decades, will affect firn densification
465 processes. Melting rounds snow grains and increases the rate of the first stage of densification. With enough melt to drive
466 meltwater percolation through the snow and firn layer, meltwater can fill in air pockets and refreeze, further accelerating the
467 transition from snow to ice (Cuffey and Paterson, 2010). The overall pattern of density measurements from 2018 resembles a
468 logarithmic densification curve (Figure 2) (Cuffey and Paterson, 2010), as is typical for Sorge’s Law of densification in dry

469 snow (Sorge, 1935, Bader, 1954). However, with increasing meltwater percolation and refreezing effects, higher densities
470 are common in the upper portions of the firn, as observed in our cores. Bezeau et al. (2013) report similar findings from the
471 Devon Ice Cap, where they found a depth-density reversal and suggest that Sorge's Law no longer holds in areas of
472 significant warming. To account for this, firn densification models are being revised to address the effects of ice layers and
473 warming temperatures on the rate of densification (Reeh, 2008; Ligtenberg et al., 2011), and other studies are revising mass
474 balance estimates based on dynamic densification rates (e.g., Schaffer et al., 2020).

475

476 **5.2 Perennial Firn Aquifer**

477 We found unequivocal evidence for a deep perennial firn aquifer on the Upper Kaskawulsh Glacier, with excess water in the
478 firn pore space below about 32 m depth. Some of this water drained during firn core acquisition (Supplemental material
479 video 1 & 2). We cannot tell whether this PFA is a new feature at this site. Borehole temperature measurements from 1964 at
480 a site close to our cores indicate temperate conditions at 15-m depth at this time (Grew and Mellor, 1966), and it is possible
481 that firn has been temperate since that time, conducive to a PFA below the depth of the annual winter cold wave. There are
482 no historical temperature measurements from greater firn depths at the site, and earlier coring efforts and radar surveys from
483 the upper Kaskawulsh, Divide, or Eclipse sites make no comment or inference about the presence of liquid water, so we
484 cannot attest to the age or origins of the PFA. It may well be a new feature.

485

486 The modelling results suggest that there are significant decadal increases in melting and refreezing since the 1960s at this
487 site, driving firn warming, increased ice content, and densification (Table 2). The firn model predicts the development of
488 wet, temperate conditions in the deep firn following the 2013 melt season, although it takes four years to fully develop
489 (Figure 6). This was triggered by meltwater penetration to 11 m depth in 2013, which is below the depth of penetration of the
490 winter cold wave. Temperate conditions propagated downwards in the following years and persisted to 2019, supported by
491 several more years with above-average melting. Deep meltwater percolation during these years would support the
492 development and recharge of a PFA or perched water table at the glacier ice-firn interface. This agrees with the stratigraphy
493 found in the field. The presence of firn that has not been visibly affected by meltwater overlying the PFA implies that deep
494 meltwater infiltration through vertical piping may be an important process here and may allow the PFA to be recharged in a
495 heavy melt season. In the model, deep recharge does not occur every summer after the establishment of a temperate firn
496 column; the summer melt still needs to break through the winter cold layer, which typically extends to 6-7 m depth (Figure
497 6). Also of interest in Figure 6 is a large melt event in 2007, which led to meltwater infiltration and warming to about 9-m
498 depth. This was similar to the 2013 melt event, but the summers of 2008 to 2010 were relatively cool (average JJA
499 temperatures of -2.8°C and melting of 111 mm w.e.), leading to refreezing in the upper 9 m of firn. Thawing of the full 35-
500 m firn column to shift it from polythermal to temperate conditions requires several years of sustained melt forcing in the
501 model.

502

503 There are significant uncertainties in the modelling, associated with the climatological forcing, surface energy balance and
504 firn model parameterizations, and initial conditions. The Supplemental Information explores these in detail, while Figure 7
505 provides an illustration of the range of simulated behaviour for different model settings. The ‘reference model’ results
506 presented in Figures 5 and 6 should be seen as just one scenario, corresponding to our best estimate of the parameter settings.
507 We lack local calibration and validation studies, so we cannot preclude different firn temperature and melt evolutions at this
508 site, particularly given the inference of Grew and Mellor (1966) that firn at 15-m depth was temperate in the mid-1960s. The
509 default model parameters and spin-up settings do not produce this; augmented warming or incoming radiation fluxes need to
510 be introduced to the ERA climatology to produce temperate firn at this time. It is possible that strong melt seasons in the
511 early 1960s created temporary temperate conditions in the upper firn column. Alternatively, the surface energy balance and
512 firn hydrological models may underestimate the amount of melting and meltwater infiltration. The one firm conclusion is
513 that the climatological and glaciological conditions on the upper Kaskawulsh Glacier are very close to the tipping point
514 between polythermal and temperate conditions. A slight nudge to either side of the reference model settings can give either
515 persistently sub-zero or persistently thawed conditions in the deep firn at this site (Figures 7 and S1).

516

517 The presence of the deep PFA in 2018 indicates that it is currently temperate, despite mean annual air temperatures of about
518 -11°C . Meltwater refreezing releases enough latent heat to bring the firn to 0°C . All model simulations concur on this,
519 although the long-term evolution is uncertain. We don’t know the fate of the water that drains through the firn, but the
520 reference model predicts a total drainage of 1.13 m w.e. over the 55-year simulation, most of this over the last decade. Some
521 of this is retained within the PFA, but some can be expected to run off. The water in the PFA on Kaskawulsh Glacier is
522 likely to be flowing, redistributing mass. The drill site was located high in the glacier’s accumulation zone, with a gently
523 sloping surface ($< 0.6^{\circ}$) resulting in a subtle hydraulic gradient. We likely drilled into the top of the water table of the PFA.
524 There may be downslope flow along the firn-ice interface, as well as possible Darcian flow within the PFA itself (e.g.,
525 Christianson et al., 2015).

526

527 The liquid-phase meltwater retention on Kaskawulsh is similar to the PFAs found in the high-accumulation areas of southern
528 Greenland and Svalbard (e.g., Miège et al., 2016; Christianson et al., 2015), and different than the water-saturated layers
529 commonly found on temperate glaciers. PFAs that have been studied on temperate mountain glaciers typically have a
530 saturated layer close to the surface (for example, 5 m below the surface at Storglaciären), have active discharge and recharge
531 processes (Fountain and Walder, 1998; Schneider, 1999; Glazyrin et al., 1977), and appear to experience seasonal drainage
532 over the winter months (Fountain, 1989, 1996; Jansson et al., 2003), likely due to high hydraulic gradients. Active water
533 flow in the firn has been observed in 19-m and 25-m pits at Abramov Glacier (Glazyrin et al., 1977), as well as Austfonna
534 ice cap in 1985 at 7 m depth where they also found sub-horizontal melt channels at 7, 15, and 30 m (Zagorodnov et al.,
535 2006). In 2012, “water-saturated” firn was found at 40-m depth in an ice core from Mt. Waddington, British Columbia (Neff
536 et al., 2012). However, they reported no significant alteration of chemistry from the melt above this layer and no additional

537 analysis of this layer was discussed (Neff et al., 2012). In 2015, a PFA was found on Holtedahlfonna icefield in Northwest
538 Svalbard (Christianson et al., 2015), and in 2019 a PFA was investigated at Lomonosovfonna ice cap approximately 100 km
539 to the southeast (Hawrylak and Nilsson, 2019).

540

541 According to Kuipers Munneke et al. (2014), PFA formation in Greenland is contingent upon a high annual snow
542 accumulation, which helps to insulate the underlying firn from the winter cold wave. Mean annual temperatures in
543 Greenland are well below 0°C and PFAs require latent heat release from meltwater refreezing, to warm the snow and firn to
544 0°C, along with meltwater penetration to depths of at least 10 m, to evade the winter cold wave (Kuipers Munneke et al.,
545 2014). The firn modelling suggests that meltwater penetration to depths of 10 m is rare at Kaskawulsh Glacier, but can occur
546 in strong melt seasons. Based on our measurements and earlier reports from the IRRP (Wood, 1963; Grew and Mellor,
547 1966), the estimated accumulation rate at our study site is 1.8 m w.e. yr⁻¹. This is similar to reported accumulation rates
548 where PFAs have been identified in southeastern Greenland (e.g., Miège et al., 2016). Melt rates at southeast Greenland PFA
549 locations are also comparable to those on the upper Kaskawulsh. Miège et al. (2016) report 0.73 m w.e. yr⁻¹ over the time
550 period 1979-2014, while Miller et al. (2020) estimate annual melt rates from 0.24-0.50 m w.e. yr⁻¹ in a PFA field study at
551 1700 m elevation in the Helheim Glacier catchment. Modelled melt rates on the upper Kaskawulsh Glacier are estimated at
552 0.52±0.27 m w.e. yr⁻¹ from 1965-2019 (Table 2). Recent (2005-2017) Kaskawulsh melt rates increased to 0.72 ± 0.38 m
553 w.e. yr⁻¹, similar to the long-term estimate of Miège et al. (2016) in southeast Greenland, and perhaps close to the threshold
554 for PFA formation and recharge.

555 **5.3 Implications for geodetic mass balance**

556 The solid and liquid phase storage mechanisms in the Kaskawulsh Glacier firn layer have different implications for the mass
557 balance of the glacier. Liquid water is commonly found in the temperate firn of low- and mid- latitude mountain glaciers and
558 has played an important role in meltwater storage and glacier hydrology (Fountain and Walder, 1989; Schneider, 1999).
559 Depending on the melt, PFA thickness, and temperature of the firn, the storage of liquid water at the firn-ice interface delays
560 runoff from hours to weeks or longer (Jansson et al., 2003). This melt can account for as much as 64% of internal
561 accumulation, as found in Alaska and Sweden (Trabant and Mayo, 1985; Schneider and Jansson, 2004).

562

563 The effects of meltwater storage through refreezing or liquid retention on high mountain glaciers complicate mass balance
564 measurements. The climate reanalysis suggests that these effects are increasing as the climate is warming. Geodetic mass
565 balance measurements are compromised by climate change-induced densification that causes surface lowering of the
566 accumulation zone (Reeh, 2008; Huss, 2013). Mass balance studies in Greenland indicate that changing melt regimes,
567 meltwater refreezing, and the unknown density and pore capacity of snow and firn pose significant uncertainties when
568 modelling the surface mass balance of large ice sheets (Lenaerts et al., 2019). Meltwater retention as porewater or refrozen
569 ice will delay surface runoff, dependent on the water storage characteristics of firn (e.g., pore space availability, water at

570 interstitial grain boundaries) (Fountain and Walder, 1989; Schneider, 1999). If ice layers become too extensive or thick, they
571 can form an ‘ice slab,’ a thick impermeable barrier that leads to enhanced surface runoff (MacFerrin et al., 2019). The
572 thickness of ice layers that prevents percolation is not well understood. For example, in Greenland 12-cm thick ice layers
573 were still permeable (Samimi et al., 2020) whereas Bell et al. (2008) reported that a 1-2 cm ice layer prevented percolation at
574 the Devon Ice Cap, Canada. These phenomena and effects are not limited to Greenland and the high Arctic. This study
575 demonstrates that Kaskawulsh Glacier also experiences meltwater storage in the form of ice layers and liquid water retention
576 (as a PFA), with potentially significant recent changes in firn structure and meltwater retention capacity. The increases in
577 firn density and ice content found on Kaskawulsh Glacier appear to be similar to other high-accumulation Arctic regions
578 (Pohjola et al., 2002; De La Peña et al., 2015; Bezeau et al., 2013).

579

580 The surface energy balance model is not observationally constrained at this site, so we don’t have quantitative confidence in
581 the modelled mass balance and melt rates, but the reconstructed trends indicate a ~70% increase in summer meltwater
582 production at this site since the 1960s, leading to increased rates of refreezing and also the onset of meltwater runoff in
583 recent years. Melt totals are well less than the annual accumulation (~1.8 m w.e.), so the site remains within the
584 accumulation area of the glacier, with most of the meltwater refreezing. Increases in annual meltwater refreezing drive
585 increased ice content and densification at this site. The modelling suggests a ~5% increase in firn density since the 1960s and
586 a doubling of the ice content, from 1.1 to 2.3 m over the full 35-m snow/firn column. Recent increases in summer melting
587 would also contribute to surface drawdown, as well as mass loss. Within the model, 96% of total meltwater refreezes over
588 the 55-year simulation, but this is reduced to 86% for the period represented by the firn core, 2005-2017. The remaining 27%
589 drains to the deep firn through this period, where it is either retained within the PFA or it may drain from the system. A total
590 of ~1.3 m w.e. ‘runs off’ through the period 2005-2017. In the model, this drains through the bottom layer and leaves the
591 system; in reality, this water may drain through lateral transport in the PFA or at the ice-firn interface.

592

593 The modelled 2018 firn core has an ice content of 2.6 m, compared to a total ice content of 2.33 ± 0.26 m measured in Core
594 1. The modelled ice content is a completely independent estimate and is in reasonable agreement with the firn core, giving
595 some confidence in the modelled refreezing, but it is about 15% in excess of the observations. This suggests that the model
596 may slightly over-estimate the melt or the meltwater infiltration. However, that inference is not consistent with the apparent
597 cold bias in the model spin-up. Alternatively, firn in the model may be too cold through much of the simulation, causing an
598 overestimate of the modelled meltwater refreezing and retention capacity. If this is the case, runoff (summer mass losses)
599 from the site will be higher than our estimates, with negative implications for Kaskawulsh Glacier mass balance.

600

601 The accumulation zone of Kaskawulsh Glacier is estimated to have experienced a minimum of 0.73 ± 0.23 m of surface
602 lowering due to internal refreezing over the period represented by Core 1, which we estimate to be 12.5 years, or 0.06 ± 0.02
603 m yr^{-1} from 2005-2017. This estimate of thinning is likely low, because neither the meltwater retention due to the infiltration

604 ice nor the presence of the PFA is included in this estimate. In previous measurements of surface elevation changes on
605 Kaskawulsh Glacier, Foy et al. (2011) found that the accumulation zone thinned by an average of 0.04-0.11 m yr⁻¹ from
606 1977-2007, with a total thinning of 1–3 m over this period. Larsen et al. (2015) reported mean elevation losses of 0-1 m yr⁻¹
607 towards the head of the glacier from 1995-2000. The thinning signal due to meltwater percolation and refreezing is within
608 the estimates of Foy et al. (2011) and Larsen et al. (2015), suggesting that some or all of the reported lowering could be due
609 to mass redistribution and not mass loss. The density of the firn has increased from 1964-2018 due to meltwater percolation
610 and refreezing. It is therefore likely that the surface has lowered since 1964 because of this increased densification.

611 **6 Conclusion**

612 The upper accumulation zone of Kaskawulsh Glacier firn has undergone significant changes since 1964. The firn has
613 become warmer, denser, and more ice-rich since 1964. The firn now contains a PFA, which has likely developed over the
614 past decade. The mean density of the first 32 m of firn (4.2 to 36.2 m below the surface) was $698 \pm 5 \text{ kg m}^{-3}$, and firn
615 densification due to meltwater refreezing into ice layers over the last ~12.5 years (2005-2017) is responsible for an estimated
616 surface lowering of $0.73 \pm 0.23 \text{ m}$. The PFA may be a recent feature, attributed to increased summer melting, meltwater
617 infiltration, and firn warming from the associated latent heat release. Our study illustrates a high elevation accumulation area
618 that is changing in response to climate-driven surface warming and provides density information required for geodetic mass
619 balance calculations.

620

621 This study has utilized historical density data in order to assess the changes in densification due to meltwater percolation and
622 refreezing since 1964. The firn of Kaskawulsh Glacier has become up to 15% denser due to the increased amount of ice
623 layers and melt-affected firn. The Kaskawulsh Glacier PFA needs to be more widely studied. The spatial extent and depth of
624 the aquifer is not yet known. Ground penetrating radar measurements may provide a method to investigate the spatial extent
625 of the feature. Use of an electrothermal drill that can drill through water-saturated firn may allow estimations of the depth of
626 the firn aquifer, as well as subsequent studies on the potential flow of the water within the aquifer. This region will likely
627 continue to experience increasing amounts of surface melt and refreezing within the snowpack and firn, so there is urgency
628 to obtain climate records from this region.

629

630 *Data availability.* Raw density data is available by contacting the corresponding author.

631

632 *Author contribution.* NO and AC collected field data. AC ran ion analyses, supervised the field campaign and helped with
633 figures. SM contributed to the design and funding of the study and was responsible for the firn modelling. BM and SM
634 provided supervision during the project. LC provided weather station data and contributed to the collection and interpretation
635 of data. NO analysed the data and wrote the manuscript, to which all co-authors contributed.

636

637 *Competing interests.* The authors declare no competing interests.

638

639 *Acknowledgements.* This work was part of a Polar Knowledge Canada Grant in support of Cryosphere-Climate Monitoring at
640 Kluane Lake Research Station, Yukon Territory. We acknowledge the Natural Sciences and Engineering Research Council
641 (NSERC) of Canada for additional financial support. We thank Parks Canada for permission to conduct this research in
642 Kluane National Park, under research and collection permit KLU-2018-28117. We are grateful for the field crew Étienne
643 Gros and Peter Moraal, Icefield Instruments Inc., for assistance with coring, and members of the University of Ottawa
644 Glaciology and Northern Field Research classes, particularly Jean Bjornson, for assistance with the snow pit measurements.
645 The Arctic Institute of North America, Kluane Lake Research Station, and Icefield Discovery supported fieldwork logistics.
646 We thank Kristina Miller, University of Calgary, for field support and countless glaciological discussions, Shad O’Neel and
647 Louis Sass of the U.S. Geological Survey for sharing firn density data from Alaska, Christian Zdanowicz, Uppsala
648 University, for sharing his 2004-2011 snow depth data from the upper Hubbard Glacier, and Eduard Khachatryan for
649 translating the Glazyrin et al. (1977) paper.

650 **References**

651 Bader, H.: Sorge’s law of densification of snow on high polar glaciers, *J. Glaciol.*, 2, 319–323, 1954.

652 Bell, C., Mair, D., Burgess, D., Sharp, M., Demuth, M., Cawkwell, F., Bingham, R. and Wadham, J.: Spatial and temporal
653 variability in the snowpack of a High Arctic ice cap: implications for mass-change measurements. *Ann. Glaciol.* 48, 159-
654 170, 2008.

655 Berthier, E., Schiefer, E., Clarke, G. K. C., Menounos, B. and Rémy, F.: Contribution of Alaskan glaciers to sea-level rise
656 derived from satellite imagery. *Nat. Geosci.* 3, 92–95, 2010.

657 Bezeau, P., Sharp, M., Burgess, D. and Gascon, G: Firn profile changes in response to extreme 21st-century melting at
658 Devon Ice Cap, Nunavut, Canada. *J. Glaciol.* 59, 981–991, 2013.

659 Christianson, K., Kohler, J., Alley, R. B., Nuth, C. and Van Pelt, W. J. J.: Dynamic perennial firn aquifer on an Arctic
660 glacier. *Geophys. Res. Lett.* 42, 1418–1426, 2015.

661 Cogley, J.G.: Geodetic and direct mass-balance measurements: comparison and joint analysis. *Ann. Glaciol.*, 50(50), 96-100,
662 2009.

663 Coleou, C., and Lesaffre, B.: Irreducible water saturation in snow: experimental results in a cold laboratory. *Ann.*
664 *Glaciol.*, 26, 64–68, <https://doi.org/10.3189/1998AoG26-1-64-68>, 1998.

665 Cuffey, K. M., and Paterson, W.: *The Physics of Glaciers* (4th ed.). Boston,: Elsevier. 1-683. 2010.

- 666 De La Peña, S, I. M. Howat, P.W. Nienow, M. R. van den Broeke, E. Mosley-Thompson, S. F. Price, D. Mair, B. Noël, and
667 A. J. Sole.: Changes in the firn structure of the western Greenland Ice Sheet caused by recent warming. *The Cryosphere*, 9,
668 1203–1211, 2015.
- 669 Ebrahimi, S. and Marshall, S. J.: Surface energy balance sensitivity to meteorological variability on Haig Glacier, Canadian
670 Rocky Mountains, *The Cryosphere*, 10, 2799–2819, <https://doi.org/10.5194/tc-10-2799-2016>, 2016.
- 671 Fountain, A. G.: The storage of water in, and hydraulic characteristics of, the firn of South Cascade Glacier, Washington
672 State, USA. *Ann. Glaciol.*, 13, 69–75. 1989.
- 673 Fountain, A. G.: Effect of Snow and Firn Hydrology on the Physical and Chemical Characteristics of Glacial Runoff.
674 *Hydrol. Process.* 10, 509–521, 1996.
- 675 Fountain, A. G. and Walder, J. S.: Water flow through temperate glaciers. *Rev. Geophys.*, 36, 299–328. 1998.
- 676 Foy, N., Copland, L., Zdanowicz, C., Demuth, and M., Hopkinson, C.: Recent volume and area changes of Kaskawulsh
677 Glacier, Yukon, Canada. *J. Glaciol.*, 57, 515–525, <https://doi.org/10.3189/002214311796905596>, 2011.
- 678 Gascon, G., Sharp, M., Burgess, D., Bezeau, P. and Bush, A. B. G.: Changes in accumulation-area firn stratigraphy and
679 meltwater flow during a period of climate warming: Devon Ice Cap, Nunavut, Canada. *J. Geophys. Res. Earth Surf.* 118,
680 2380–2391, 2013.
- 681 Grew, E., and Mellor, M.: High snowfields of the St. Elias Mountains, Yukon Territory, Canada. Hanover, N.H. U.S. Army
682 Materiel Command, Cold Regions Research & Engineering Laboratory Technical Report, 177, 1-26, 1966.
- 683 Glazyrin G.E., Glazyrina E.L., Kislov B.V. and Pertzinger F.I. Water level regime in deep firn pits on Abramov glacier [in
684 Russian], volume 45. *Gidrometeoizdat*, 2017.
- 685 Harper, J., Humphrey, N., Pfeffer, W. T., Brown, J., and Fettweis, X.: Greenland ice-sheet contribution to sea-level rise
686 buffered by meltwater storage in firn. *Nature*, 491, 240–243, 2012.
- 687 Harper, J., Humphrey, N., Pfeffer, T. and Brown, J.: Firn Stratigraphy and Temperature to 10 m Depth in the Percolation
688 Zone of Western Greenland, 2007 – 2009. Institute of Arctic and Alpine Research, University of Colorado, Occasional Paper
689 60, 2011.
- 690 Hawrylak, M., and Nilsson, E.: Spatial and Temporal Variations in a Perennial Firn Aquifer on Lomonosovfonna, Svalbard.
691 Uppsala University Independent Project, 2019. <http://www.diva-portal.se/smash/get/diva2:1319193/FULLTEXT01.pdf>.
- 692 Hersbach, H., Bell, B., Berrisford, P. et al.: The ERA5 global reanalysis. *Quarterly Journal of the Royal Meteorological*
693 *Society*, <https://doi.org/10.1002/qj.3803>, 2020.
- 694 Holdsworth, G.: An Examination and Analysis of the Formation of Transverse Crevasses, Kaskawulsh Glacier, Yukon
695 Territory, Canada. Institute of Polar Studies, 16, 1965.
- 696 Humphrey, N. F., Harper, J. T., and Pfeffer, W. T.: Thermal tracking of meltwater retention in Greenland’s accumulation
697 area. *J. Geophys. Res.*, 117, F01010, <https://doi.org/10.1029/2011JF002083>, 2012.
- 698 Huss, M.: Density assumptions for converting geodetic glacier volume change to mass change, *The Cryosphere*, 7, 219–244.
699 2013.

- 700 Jansson, P., Hock, R. and Schneider, T.: The concept of glacier storage: A review. *J. Hydrol.*, 282, 116–129, 2003.
- 701 Koenig, L. S., Miège, C., Forster, R. R. and Brucker, L.: Initial in situ measurements of perennial meltwater storage in the
702 Greenland firn aquifer. *Geophys. Res. Lett.* 41, 81–85, 2014.
- 703 Koerner, R. M.: Devon Island Ice Cap: Core Stratigraphy and Paleoclimate. *Science*, 146, 347–353. 1977.
- 704 Kuipers Munneke, P. K., Ligtenberg, S. R. M., Van Den Broeke, M. R., Van Angelen, J. H. and Forster, R. R.: Explaining
705 the presence of perennial liquid water bodies in the firn of the Greenland Ice Sheet. *Geophys. Res. Lett.* 41, 476–483, 2014.
- 706 Larsen, C. F., Burgess, E., Arendt, A. A., O'Neel, S., Johnson, A. J., and Kienholz, C.: Surface melt dominates Alaska
707 glacier mass balance. *Geophys. Res. Lett.* 42, 5902–5908. <https://doi.org/10.1002/2015GL064349>, 2015.
- 708 Lenaerts, J. T. M., Medley, B., van den Broeke, M. R. and Wouters, B.: Observing and Modeling Ice Sheet Surface Mass
709 Balance. *Rev. Geophys.* 57, 376–420, <https://doi:10.1029/2018RG000622>, 2019.
- 710 Ligtenberg, S. R. M., Helsen, M. M., and van den Broeke, M. R.: An improved semi-empirical model for the densification of
711 Antarctic firn, *The Cryosphere*, 5, 809–819, doi:10.5194/tc-5-809-2011, 2011.
- 712 Machguth, H., MacFerrin, M., van As, D., Jason E. Box, Charalampos Charalampidis, William Colgan, Robert S. Fausto,
713 Harro AJ Meijer, Ellen Mosley-Thompson, and Roderik SW van de Wal.: Greenland meltwater storage in firn limited by
714 near-surface ice formation. *Nature Clim Change*, 6, 390–393. <https://doi.org/10.1038/nclimate2899>, 2016.
- 715 MacFerrin, M. Machguth H, van As, D. C. Charalampidis, C., C. M. Stevens, C.M., Heilig, A., Vandecrux, B., P. L. Langen,
716 P. L., Mottram, R., Fettweis, X., van den Broeke, M. R., Pfeffer, W. T., M. S. Moussavi, M. S., and Abdalati. W.: Rapid
717 expansion of Greenland's low-permeability ice slabs. *Nature*, 573, 403–407, 2019.
- 718 Marcus, M. G. and Ragle, R. H. Snow accumulation in the Icefield Ranges, St. Elias Mountains, Yukon. *Arctic and Alpine*
719 *Research*, 2(4), 277-292, 1970.
- 720 Miège, C., Forster, R., Brucker, L., Koenig, L., Solomon, D.K., Paden, J. D., Box, J. E., Burges, E. W., Miller, J. Z.,
721 McNERNEY, L., Brautigam, N., Fausto, R. S., and Gogineni, S.: Spatial extent and temporal variability of Greenland firn
722 aquifers detected by ground and airborne radars. *J. Geophys. Res. Earth Surf*, 121, 2381–2398,
723 <https://doi.org/10.1002/2016JF003869>, 2016.
- 724
- 725 Miller, O., Solomon, D. K., Miège, C., Koenig, L., Forster, R., Schmerr, N. et al. : Hydrology of a perennial firn aquifer in
726 southeast Greenland: An overview driven by field data. *Water Resources Research*, 56, e2019WR026348. [https://doi.org/](https://doi.org/10.1029/2019WR026348)
727 [10.1029/2019WR026348](https://doi.org/10.1029/2019WR026348), 2020.
- 728
- 729 Moholdt, G., Nuth, C., Hagen, J. O. and Kohler, J.: Recent elevation changes of Svalbard glaciers derived from ICESat laser
730 altimetry. *Remote Sens. Environ.*, 114, 2756–2767, 2010a.
- 731
- 732 Moholdt, G., Hagen, J. O., Eiken, T. and Schuler, T. V.: Geometric changes and mass balance of the Austfonna ice cap,
733 Svalbard. *The Cryosphere*, 4, 21–34, 2010b.
- 734 Neff, P. D., Steig, Eric J., Clark, Douglas H., McConnell, Joseph R., Pettit, Erin C., and Menounos, Brian.: Ice-core net snow
735 accumulation and seasonal snow chemistry at a temperate-glacier site: Mount Waddington, southwest British Columbia,
736 Canada. *J. Glaciol.* 58(212), 1165-1175. <https://doi:10.3189/2012JoG12J078>, 2012.

- 737 Noël, B., van de Berg, W.J., Lhermitte, S., Wouters, B., Schaffer, N. and van den Broeke, M.R., 2018. Six decades of glacial
738 mass loss in the Canadian Arctic Archipelago. *J. Geophys. Res. Earth Surf.*, 123(6), 1430-1449.
739 <https://doi.org/10.1029/2017JF004304>, 2018.
- 740 Noël, B., Jakobs, C.L., van Pelt, W.J.J., Lhermitte, S., Wouters, B., Kohler, J., Hagen, J.O., Luks, B., Reijmer, C.H., Van de
741 Berg, W.J. and van den Broeke, M.R.: Low elevation of Svalbard glaciers drives high mass loss variability. *Nat Commun.*,
742 11(1), 1-8. <https://doi.org/10.1038/s41467-020-18356-1> 2020.
- 743 Parry, V., Nienow, P., Mair, D., Scott, J., Hubbard, B., Steffen, K., and Wingham, D.: Investigations of meltwater refreezing
744 and density variations in the snowpack and firn within the percolation zone of the Greenland ice sheet. *Ann. Glaciol.* 61–68.
745 2007.
- 746 Pohjola, V. A., Moore, J. C., Isaksson, E., Jauhiainen, T., van de Wal, R. S. W., Martma, T., Meijer, H. A. J., and Vaikmäe,
747 R.: Effect of periodic melting on geochemical and isotopic signals in an ice core from Lomonosovfonna, Svalbard. *J.*
748 *Geophys. Res.*, 107, 4036, 2002.
- 749 Poli, P., Hersbach, H., Dee, D. P. and 12 others.: ERA-20C: An atmospheric reanalysis of the 20th century. *J. Climate*, 29
750 (11), 4083-407, <https://doi.org/10.1175/JCLI-D-15-0556.1>, 2016.
- 751 Reeh, N.: A nonsteady-state firn-densification model for the percolation zone of a glacier, *J. Geophys. Res.*, 113,
752 F03023,doi:10.1029/2007JF000746, 2008.
- 753 Rohatgi, A., WebPlotDigitizer. Version 4.3. 2020. <https://automeris.io/WebPlotDigitizer>
- 754 Samimi, S. and Marshall, S. J.: Diurnal cycles of meltwater percolation, refreezing, and drainage in the supraglacial
755 snowpack of Haig Glacier, Canadian Rocky Mountains. *Front. Earth Sci.* 5, 1–15. <https://doi.org/10.3389/feart.2017.00006>,
756 2017.
- 757 Samimi, S., Marshall, S. J., and MacFerrin, M.: Meltwater penetration through temperate ice layers in the percolation zone at
758 DYE-2, Greenland Ice Sheet. *Geophys. Res. Lett.*, 47, e2020GL089211. 2020.
- 759 Schaffer, N., Copland, L., Zdanowicz, C., Burgess, D., & Nilsson, J.: Revised estimates of recent mass loss rates for Penny
760 Ice Cap, Baffin Island, based on 2005–2014 elevation changes modified for firn densification *J. Geophys. Res. Earth Surf.*
761 125, e2019JF005440. 2020. <https://doi.org/10.1029/2019JF005440>
- 762 Schneider, T.: Water movement in the firn of Storglaciären. *J. Glaciol.* 45, 286–294, 1999.
- 763 Schneider, T. & Jansson, P. Internal accumulation in firn and its significance for the mass balance of Storglaciären, Sweden.
764 *J. Glaciol.* 50, 25–34, 2004.
- 765 Sorge, E. (1935). Glaziologische Untersuchungen in Eismitte. Wissenschaftliche Ergebnisse der Deutschen Gronland-
766 Expedition Alfred-Wegener 1929 und 1930-1931, 3, 270. in: K. Wegener, im Auftrag der Notgemeinschaft der Deutschen
767 Wissenschaft (Ed.), Band III, Glaziologie, 1935.
768
- 769 Trabant, D. C. and Mayo, L. R.: Estimation and effects of internal accumulation on five glaciers in Alaska. *Ann. Glaciol.*, 6,
770 113–117, 1985.
- 771 van As, D., Box, J. E., and Fausto, R. S.: Challenges of Quantifying Meltwater Retention in Snow and Firn: An Expert
772 Elicitation., *Front. Earth Sci.* 4(101), <https://doi.org/10.3389/feart.2016.00101>, 2016.

- 773 van Pelt, W., Pohjola, V., Pettersson, R., Marchenko, S., Kohler, J., Luks, B., Hagen, J. O., Schuler, T. V., Dunse, T., Noël,
774 B., and Reijmer, C.: A long-term dataset of climatic mass balance, snow conditions, and runoff in Svalbard (1957–2018),
775 *The Cryosphere*, 13, 2259–2280, <https://doi.org/10.5194/tc-13-2259-2019>, 2019.
- 776 Wagner, P. W.: Description and evolution of snow and ice features and snow surface forms on the Kaskawulsh Glacier.
777 *Icefield Ranges Research Project: Scientific Results*, 1, 51–53, 1969.
- 778 Vionnet, V., Brun, E., Morin, S., Boone, A., Faroux, S., Le Moigne, P., et al.: The detailed snowpack scheme Crocus and its
779 implementation in SURFEX v7.2. *Geosci. Model Dev.* 5, 773–791, doi: 10.5194/gmd-5-773-2012, 2012.
- 780 Williamson, S., Zdanowicz, C., Anslow, F., S. Clarke, G. K. C., Copland, L., Danby, R. K., Flowers, G. E., Holdsworth, G.,
781 Jarosch, A. H., and Hik, D. S.: Evidence for elevation-dependent warming in the St. Elias Mountains, Yukon, Canada. *J.*
782 *Clim.* 3253–3269, <https://doi:10.1175/jcli-d-19-0405.1>, 2020.
- 783 Wood, W. A.: The Icefield Ranges Research Project. *Geo. Rev.*, 53, 503–529. <https://doi.org/10.1126/science.15.370.195>,
784 1963.
- 785 Yalcin, K., Wake, C. P., Kreutz, K. J., and Whitlow, S. I.: A 1000-yr record of forest fire activity from Eclipse Icefield,
786 Yukon, Canada. *The Holocene*, 16(2), 200–209, <https://doi.org/10.1191/0959683606h1920rp>, 2006.
- 787 Young, E. M., Flowers, G. E., Berthier, E. and Latto, R.: An imbalancing act: the delayed dynamic response of the
788 Kaskawulsh Glacier to sustained mass loss. *Journal of Glaciology*, 18 pp, <https://doi.org/10.1017/jog.2020.107>, 2020.
- 789 Zagorodnov, V., Nagornov, O., and Thompson, L: Influence of air temperature on a glacier’s active-layer temperature.
790 *Annals of Glaciology*, 43, 285–291. doi:10.3189/172756406781812203, 2006.
- 791 Zdanowicz, C., Smetny-Sowa, A., Fisher, D., Schaffer, N., Copland, L., Eley, J., and Dupont, F.: Summer melt rates on
792 Penny Ice Cap, Baffin Island: Past and recent trends and implications for regional climate. *J. Geophys. Res. Earth Surf*, 117,
793 F02006, <https://doi:10.1029/2011JF002248>, 2012.
- 794 Zdanowicz, C., Fisher, D., Bourgeois, J., Demuth, M., Sheng, J., Mayewski, P., Kreutz, K., Osterberg, E., Yalcin, K., Wake,
795 C., Steig, E., Froese, D., and Goto-Azuma, K.: Ice cores from the St. Elias Mountains, Yukon, Canada: Their significance for
796 climate, atmospheric composition and volcanism in the North Pacific region. *Arctic*, 1–23, 2014.
- 797

798

799

800 **Table 1:** Total ice content, ice fraction (F_i), bulk density (ρ_b) and background density (ρ_f), for the firn portion of each core.
 801 Depths are reported from the May 2018 snow surface and the firn portion of the core started at the 2017 summer surface, at
 802 4.2 m depth.

803

	Depth below surface (m)	Total Ice content (m)	F_i (% vol)	F_i (% mass)	ρ_b (kg m^{-3})	ρ_f (kg m^{-3})	w w.e. (m)
Core 1	4.2-14.2	0.67 ± 0.07	6.7 ± 0.7	13.0 ± 1.3	588 ± 8	565 ± 9	5.88 ± 0.08
	4.2-21.6	1.51 ± 0.15	8.7 ± 0.9	15.6 ± 1.6	640 ± 6	613 ± 7	11.08 ± 0.11
	4.2-36.6	2.33 ± 0.26	7.2 ± 0.7	11.9 ± 1.2	698 ± 5	676 ± 6	22.49 ± 0.15
Core 2	4.2-14.2	0.42 ± 0.04	4.2 ± 0.4	8.4 ± 0.8	572 ± 7	556 ± 7	5.72 ± 0.07
	4.2-21.6	0.81 ± 0.08	4.7 ± 0.5	8.5 ± 0.9	624 ± 5	609 ± 6	10.85 ± 0.09
Average	4.2-14.2	1.18	4.0	564	580 ± 5	560 ± 5	5.80 ± 0.05
	4.2-21.6				632 ± 4	611 ± 4	10.97 ± 0.07

804

805

806

807

808 **Table 2:** Climate, surface energy balance, and firn conditions, 1965 to 2019, based on the ERA meteorological forcing at the
 809 core site. Decadal trends are reported from linear fits to the data. The period 1965-1975 represents the historical baseline
 810 period, when much of the work of the IRRP was completed. 2005-2017 represents the period of record of Core 1, and 2013
 811 was an exceptional year which potentially marked the initial development of the firn aquifer at this site. Melt and refreeze
 812 refer to the total annual melting and refreezing in the 35-m snow and firn column, ‘drainage’ is the total annual melt minus
 813 refreezing, and ‘net melt’ refers to the net surface melting minus refreezing, accounting for meltwater freeze-thaw cycles.
 814 This is the actual surface drawdown associated with summer melting.

815

816

817

818

819

820

821

822

823

824

825

826

827

828

829

830

831

832

833

834

835

836

837

838

839

840

841

842

843

844

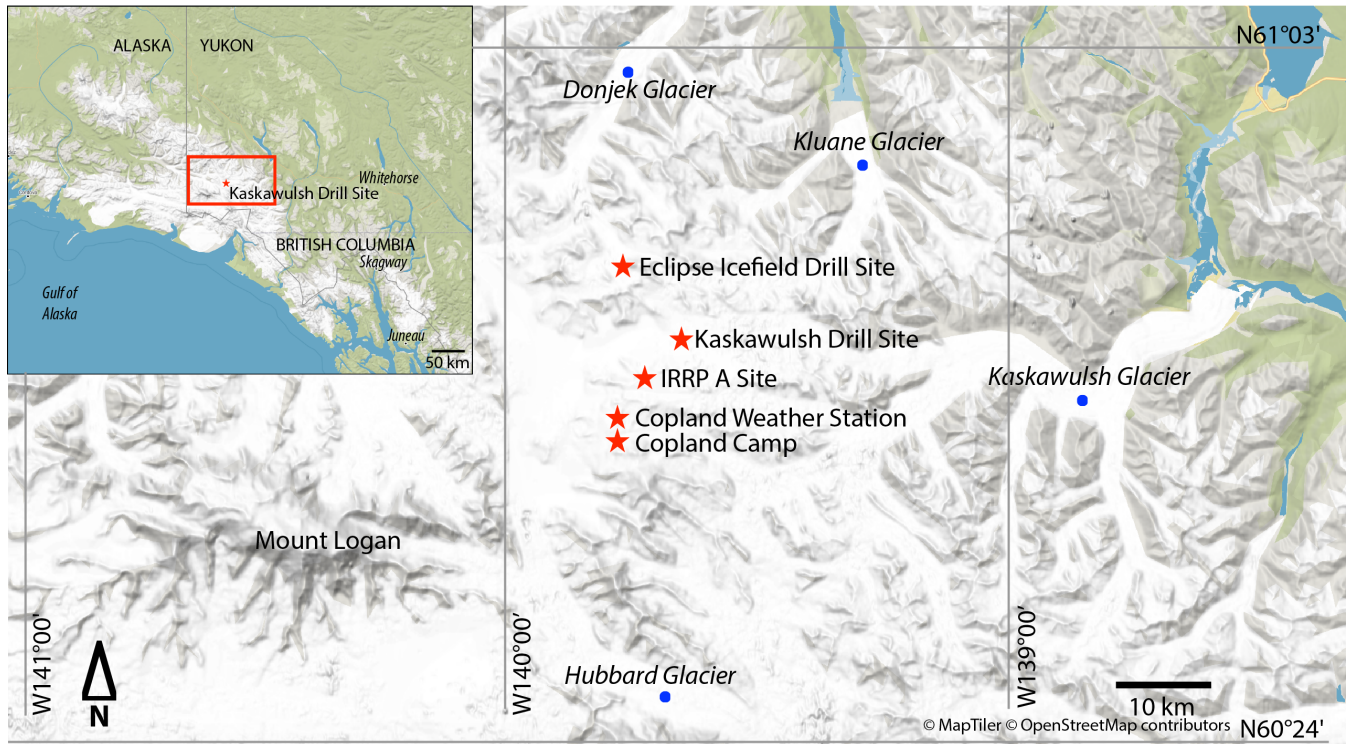
845

846

847

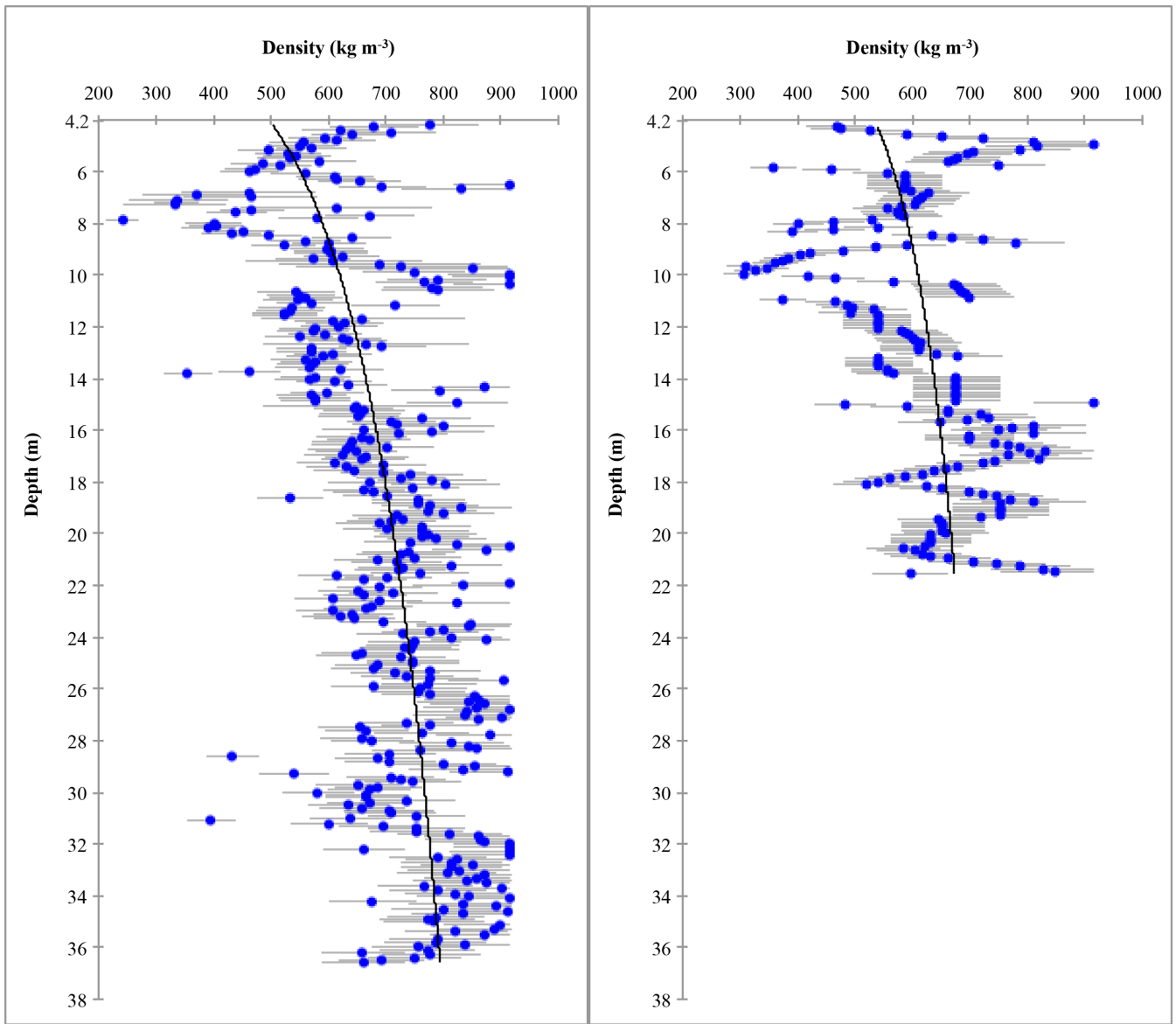
848

	1965-2019 Mean ($\pm 1 \sigma$)	Trend (decade ⁻¹)	1965-1975 Mean ($\pm 1 \sigma$)	2005-2017 Mean ($\pm 1 \sigma$)	2013
<i>Meteorological Conditions</i>					
T_{ann} (°C)	-10.7 ± 0.9	+0.16	-11.2 ± 0.7	-10.4 ± 1.0	-9.6
T_{JJA} (°C)	-2.4 ± 0.8	+0.07	-2.2 ± 0.9	-2.1 ± 0.7	-0.7
T_{SJJJ} (°C)	-2.3 ± 0.8	+0.29	-2.9 ± 0.9	-1.8 ± 0.6	-0.8
PDD (°C d)	54 ± 23	+3.6	49 ± 16	69 ± 31	123
q_v (g kg ⁻¹)	3.7 ± 0.2	+0.10	3.5 ± 0.2	3.9 ± 0.2	4.2
<i>Surface Energy Balance (JJA values)</i>					
Q^* (W m ⁻²)	18 ± 11	+3.7	8 ± 3	26 ± 13	45
Q_N (W m ⁻²)	10 ± 9	+2.6	4 ± 3	16 ± 13	37
net melt (mm w.e. yr ⁻¹)	230 ± 210	+62	100 ± 80	380 ± 310	895
melt (mm w.e. yr ⁻¹)	520 ± 270	+81	360 ± 130	720 ± 375	1360
refreeze (mm w.e. yr ⁻¹)	500 ± 195	+48	360 ± 130	615 ± 205	1100
drainage (mm w.e. yr ⁻¹)	20 ± 120	+32	0 ± 0	105 ± 215	260
<i>Firn Conditions</i>					
T_1 (°C)	-12.8 ± 0.9	+0.2	-13.3 ± 0.8	-12.4 ± 0.9	-11.5
T_{10} (°C)	-7.3 ± 3.4	+1.8	-11.3 ± 0.8	-2.9 ± 2.4	-3.0
T_{20} (°C)	-7.2 ± 3.6	+2.1	-12.2 ± 0.5	-3.7 ± 2.5	-4.5
T_{35} (°C)	-8.0 ± 3.5	+2.1	-12.7 ± 0.4	-4.8 ± 1.9	-5.2
z_{thaw} (m)	6.8 ± 9.4	+3.6	1.2 ± 1.0	13.1 ± 12.5	18.0
E_{lat} (MJ m ⁻²)	126 ± 41	+9.3	98 ± 30	147 ± 43	258
ρ_b (kg m ⁻³)	655 ± 10	+4.6	645 ± 3	663 ± 12	671
ice content (m)	2.0 ± 0.6	+0.2	1.1 ± 0.3	2.3 ± 0.4	2.6



850
851

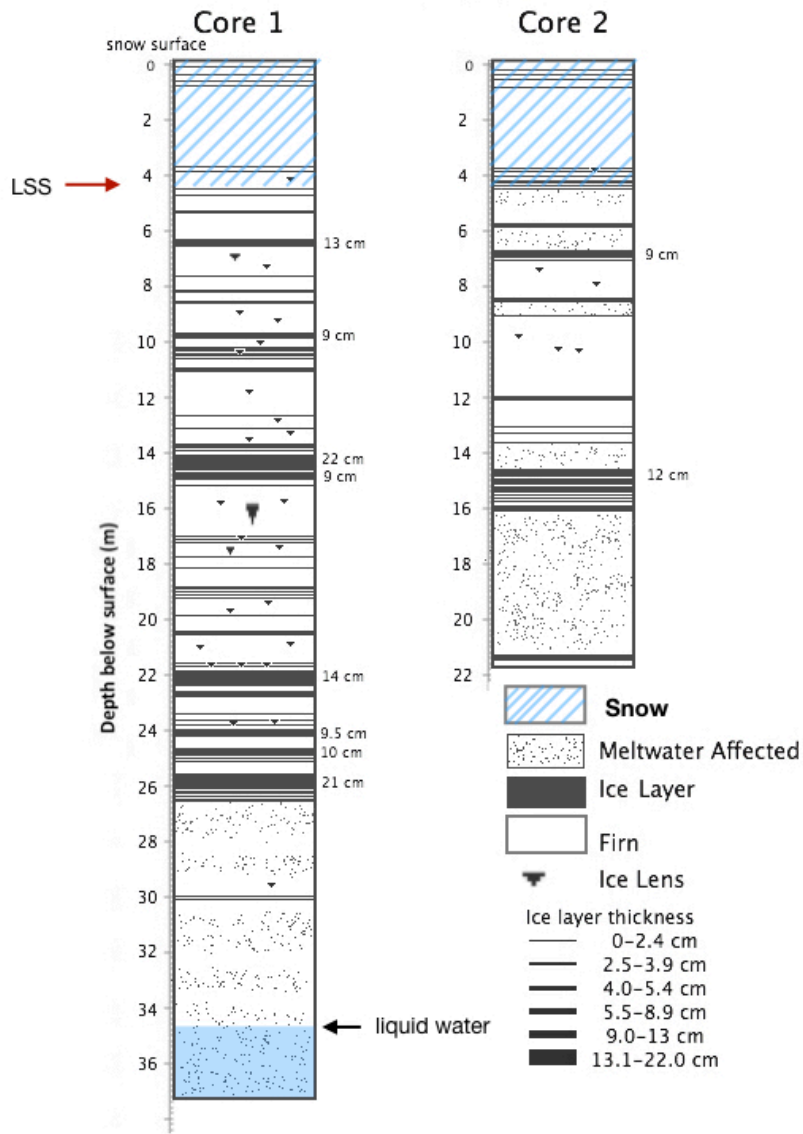
852 **Figure 1:** Field locations in the St. Elias Icefield, Yukon. IRRP A site is the site of the 1964 firn core that is referenced in
853 our study (Grew and Mellor, 1966). Base map from <http://openmaptiles.org/>.



854

855 **Figure 2:** Measured firn densities of: (A) Core 1, and (B) Core 2 (May 20-24th 2018), with uncertainties and best-fit
 856 logarithmic curves (black line). The depth scales are truncated at the location of the last summer surface at 4.2 m depth, as
 857 the profile consisted of seasonal snow above this.

Firn Stratigraphy and Density



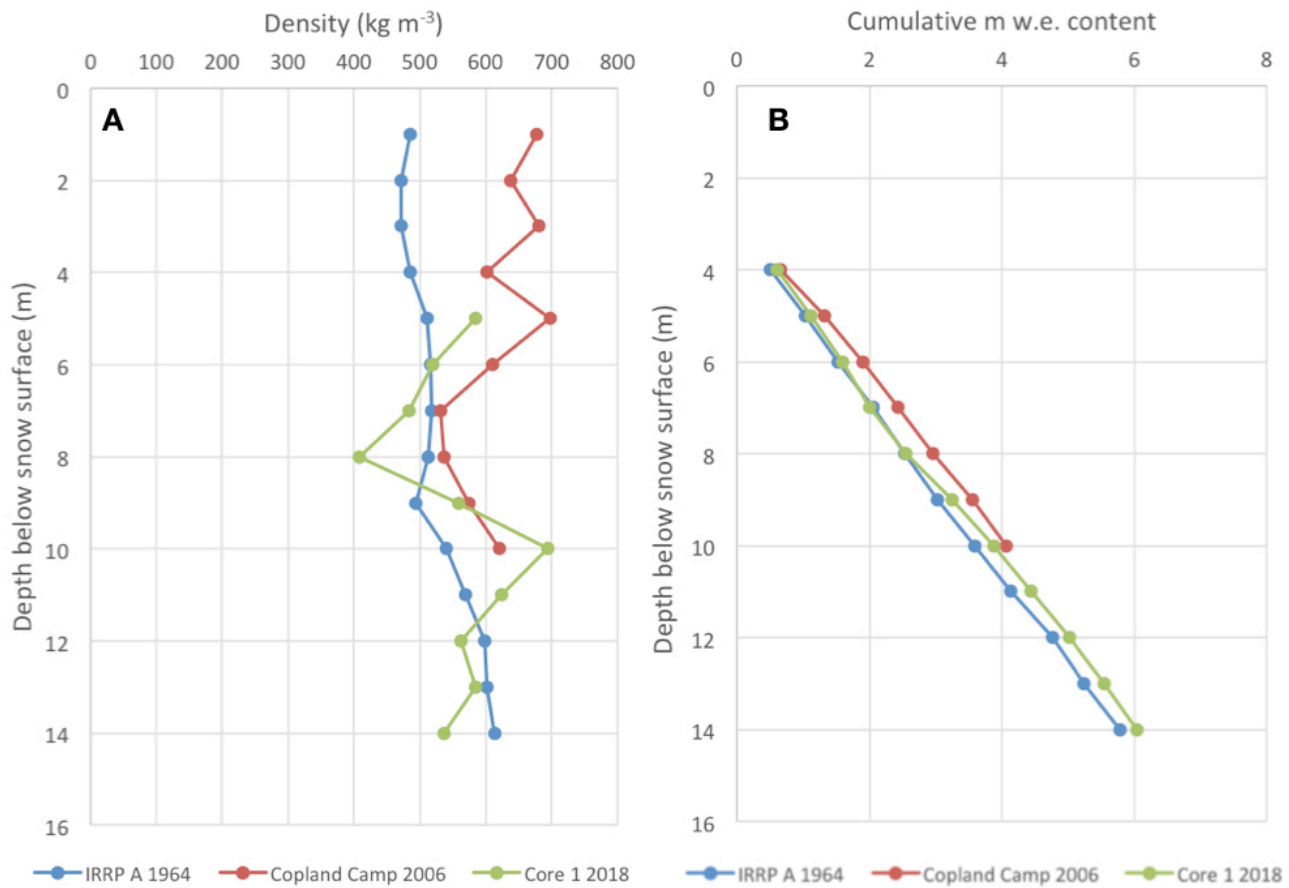
858

859 **Figure 3:** Stratigraphy of the cores collected in May 2018. LSS is the last summer surface, the boundary between seasonal
 860 snow above and firn below. Ice layer thicknesses were classified in the legend by thickness distribution. Note that the ice
 861 layers in the first several meters of the core are interpreted as wind crusts.

862

863

864



866

867

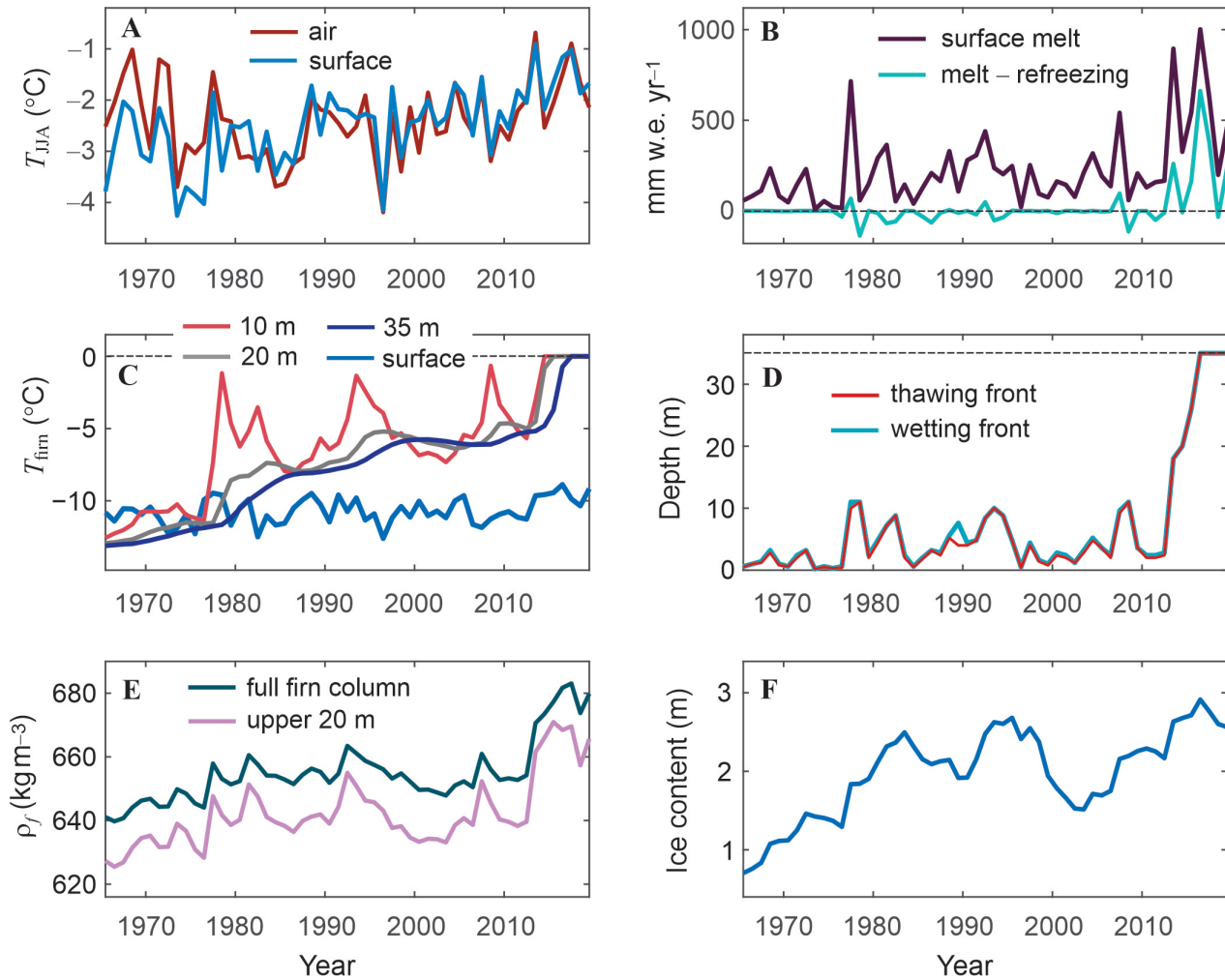
868 **Figure 4:** A) Comparison of densities averaged over 1 m segments at IRRP A on July 23, 1964 (Grew and Mellor, 1966;
 869 blue); at Copland Camp on July 14-17, 2006 (red); at Core 1 on May 20-24, 2018 (green). Depth of LSS (i.e., boundary
 870 between seasonal snow above and firn below) was 3.28 m in 1964, 3.50 m in 2006, and 4.22 m in 2018; the density data for
 871 2018 begins at the LSS due to the difference in time of year of the measurements compared to the others; B) Comparison
 872 between cumulative w.e. content in the 1964, 2006 and 2018 profiles, starting at the LSS.

873

874

875

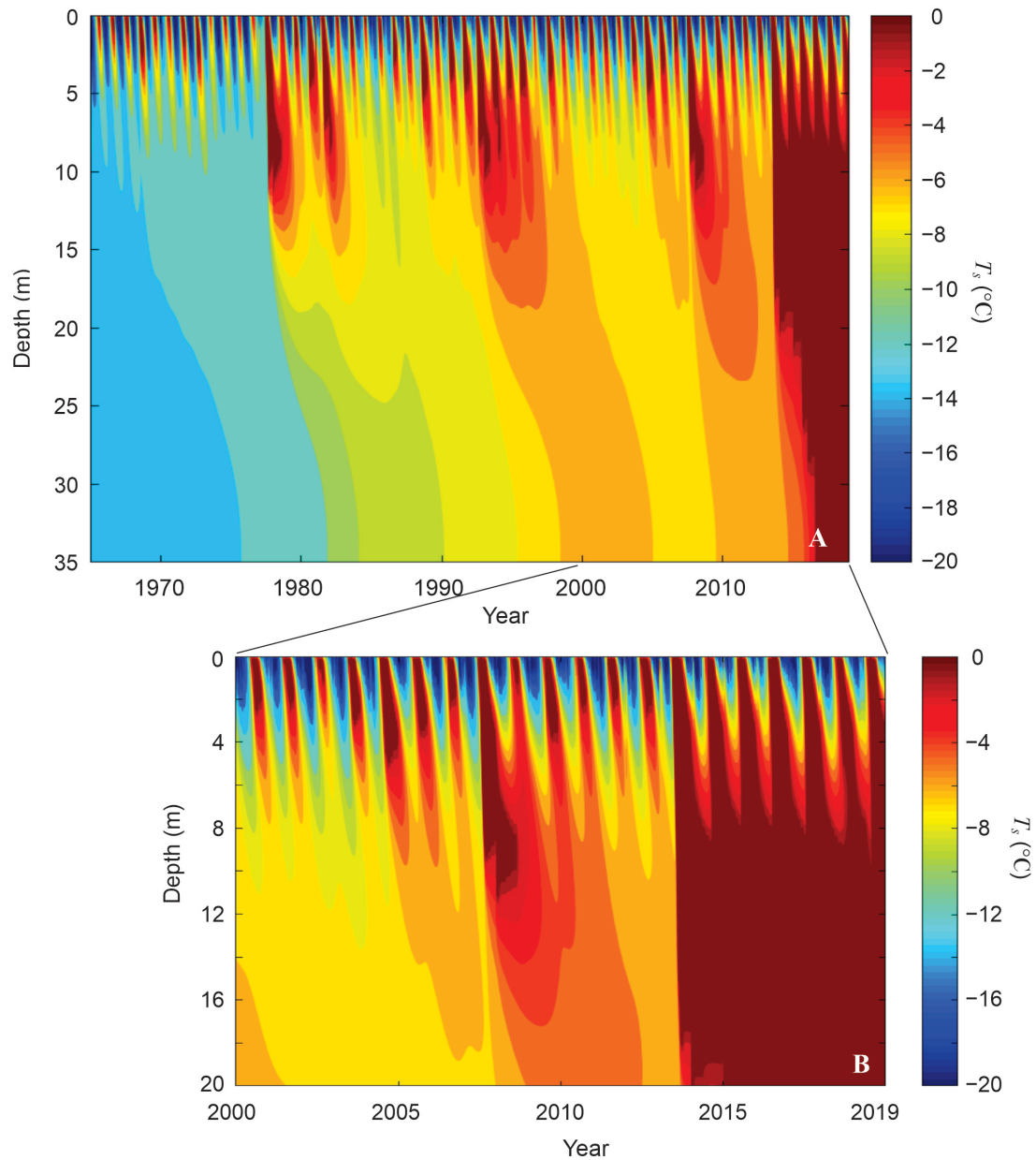
876
877
878



879
880

881 **Figure 5:** Modelled meteorological, surface mass balance, and firn conditions from 1965 to 2019: (A) Summer (JJA) air and
882 snow-surface temperatures, $^{\circ}\text{C}$; (B) Annual melting and 'drainage' (melting minus refreezing), mm w.e. yr^{-1} ; (C) Annual
883 mean snow and firn temperature at the surface (0.1 m) and at depths of 10, 20, and 35 m, $^{\circ}\text{C}$; (D) Modelled maximum depths
884 of the summer wetting and thawing fronts, m; (E) Average firn density for the full firn column and in the upper 20 m, kg m^{-3} ;
885 (F) total firn ice content, m.

886



888

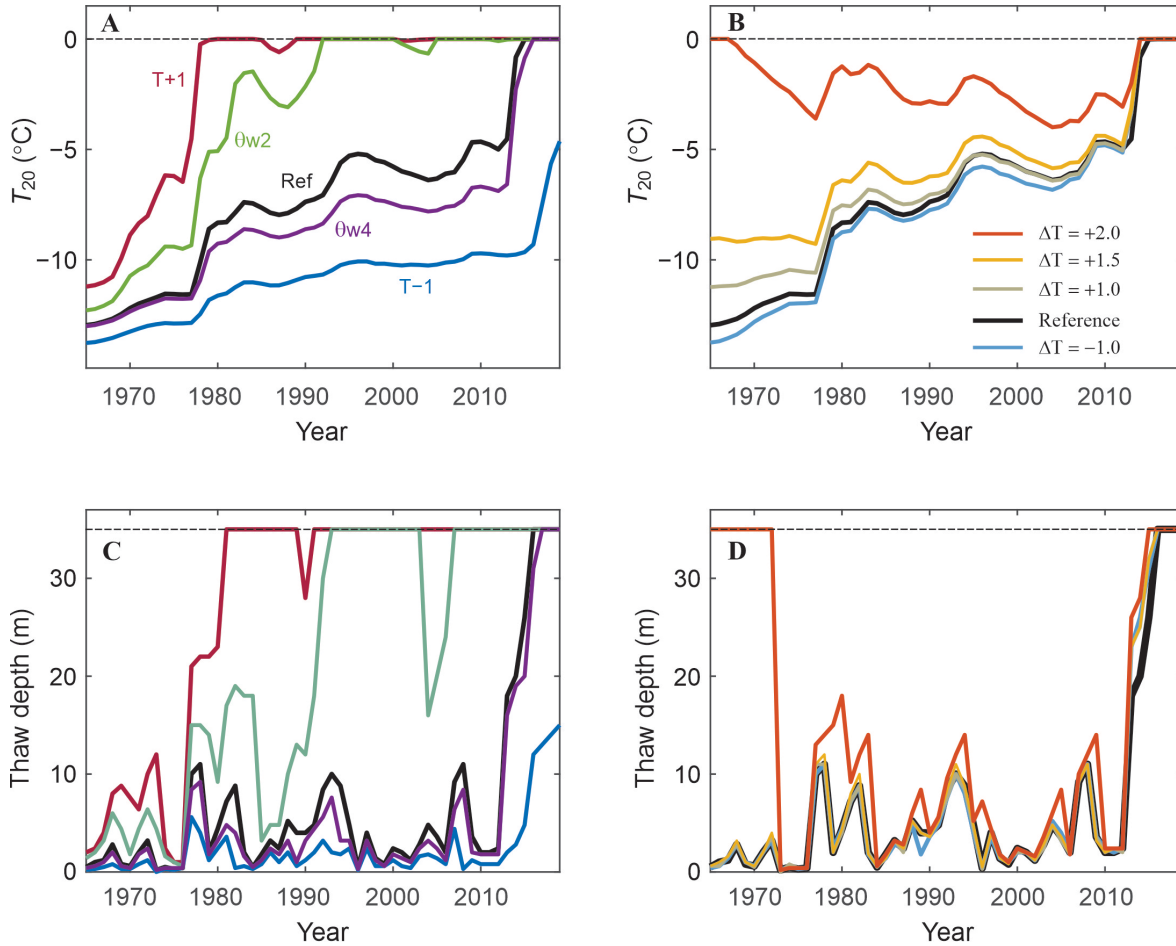
889

890 **Figure 6:** Modelled subsurface temperature evolution for the reference model climatology and parameter settings. (A) 1965-
 891 2019, full 35-m firn column; (B) 2000-2019, upper 20 m. Deep temperate conditions conducive to a firn aquifer developed
 892 from 2013 to 2017, in response to several subsequent summers of high melting and deep meltwater infiltration.

893

894

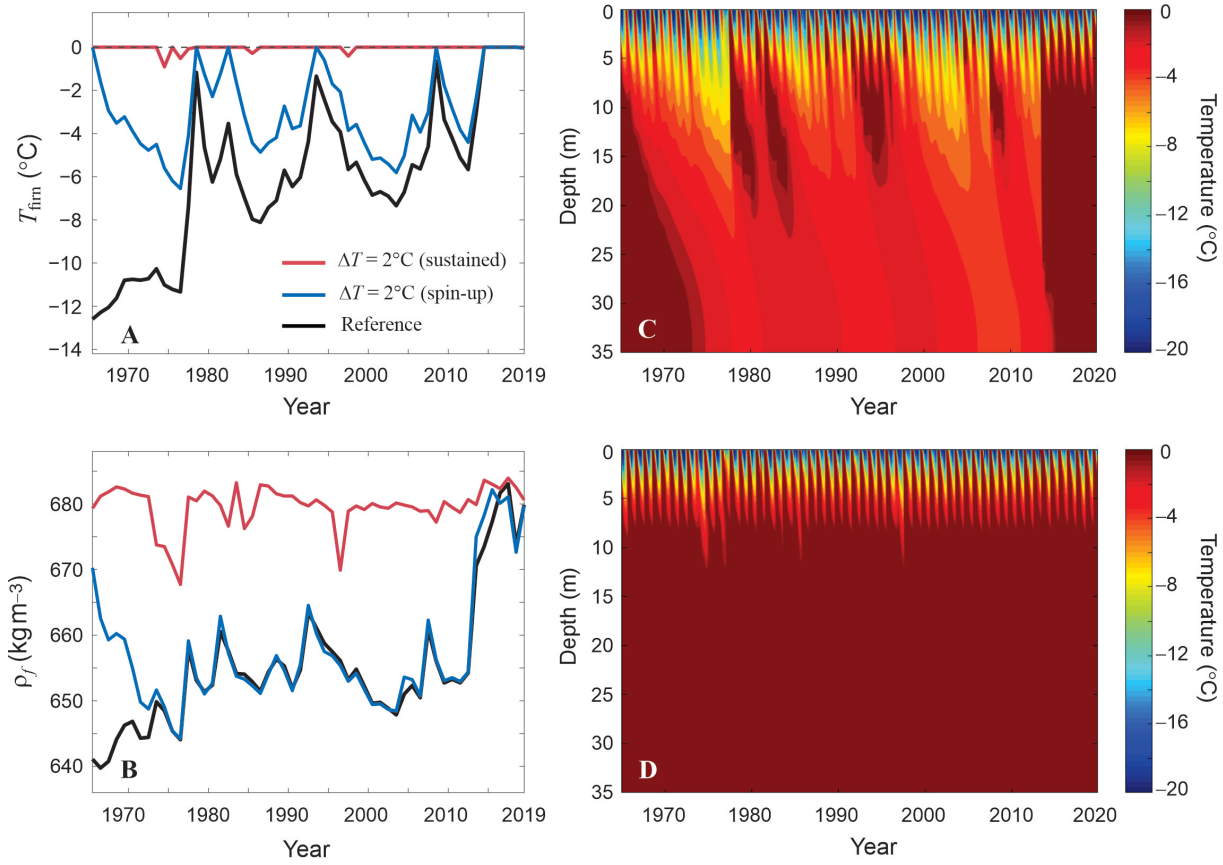
895
896
897
898



899
900

901 **Figure 7:** Sensitivity of the model simulations to (A,C) meteorological forcing and firm model parameters, and (B,D) initial
902 conditions, through different model spin-up settings. (A) Mean annual 20-m temperatures and (C) seasonal thaw depths from
903 1965-2019 for the reference model and for sensitivity experiments with $\pm 1^\circ\text{C}$ and for irreducible water contents of 0.02
904 ($\theta w2$) and 0.04 ($\theta w4$). The line colours in (A) also apply to (C). An extended set of sensitivity tests is presented in the
905 supplementary material. (B) 20-m temperatures and (D) thaw depths from 1965-2019 after a 30-year spin-up with perpetual
906 1965 climatology (the reference model) and imposed temperature anomalies of 1, 1.5, 2, and 2.5°C for the spin-up. The
907 colour legend for (B) and (D) is indicated in (B).

908
909



911

912

913 **Figure 8:** Modelled (A) 10-m firn temperature and (B) average firn density for the reference model, for a 2°C temperature
 914 anomaly for the spin-up, and for a sustained temperature anomaly of $+2^{\circ}\text{C}$. (C,D) Firn temperature evolution for (C) the
 915 warm spin-up, followed by the reference climatology, and (D) sustained 2°C temperature anomalies.

916